Materials Chemistry and Physics 328 (2024) 129943

Contents lists available at ScienceDirect

Materials Chemistry and Physics

journal homepage: www.elsevier.com/locate/matchemphys

Structural, morphological, and magnetic characterizations of $(Fe_{0.25}Mn_{0.75})_2O_3$ nanocrystals: A comprehensive stoichiometric determination

John C. Mantilla [a,b,*], Luiz C.C.M. Nagamine [b,**], Daniel R. Cornejo [b], Renato Cohen [b], Wesley de Oliveira [c], Paulo E.N. Souza [d], Sebastião W. da Silva [d], Fermin F.H. Aragón [d,e], Pedro L. Gastelois [f], Paulo C. Morais [g,h], José A.H. Coaquira [d]

[a] *Universidade Federal de Uberlândia, Instituto de Física, Uberlândia, MG, 38408-100, Brazil*
[b] *Universidade de São Paulo, Instituto de Física, São Paulo, SP, 05508-090, Brazil*
[c] *Universidade Federal de Mato Grosso do Sul, Instituto de Física, Campo Grande, MS, 79070-900, Brazil*
[d] *Universidade de Brasília, Instituto de Física, Núcleo de Física Aplicada, Brasília, DF, 70910-900, Brazil*
[e] *Departamento de Ciencias, Sección Física, Pontificia Universidad Católica del Perú, Av. Universitaria 1801, San Miguel, Lima, 32, Peru*
[f] *Centro de Desenvolvimento da Tecnologia Nuclear – CDTN, Av. Antônio Carlos, 6627, Pampulha, Belo Horizonte, MG, 31270-90, Brazil*
[g] *Universidade Católica de Brasília, Programa de Pós-Graduação em Ciências Genômicas e Biotecnologia, Brasília, DF, 70790-160, Brazil*
[h] *Centro Internacional de Física, Instituto de Física, Universidade de Brasília, Brasília, DF, 70910-900, Brazil*

* Corresponding author. Universidade Federal de Uberlândia, Instituto de Física, Uberlândia, MG, 38408-100, Brazil.
** Corresponding author.
E-mail addresses: mantilla52@gmail.com (J.C. Mantilla), nagamine@if.usp.br (L.C.C.M. Nagamine), ffharagon@gmail.com (F.F.H. Aragón).

https://doi.org/10.1016/j.matchemphys.2024.129943

Available online 13 September 2024

HIGHLIGHTS

- Essentially, two distinct nanophases, namely the primary $(Fe_xMn_{1-x})_2O_3$ and secondary α-Fe_2O_3 were successfully synthesized by the sol-gel method.
- Through Mössbauer spectroscopy analysis and Rietveld refinement of X-ray diffraction data, the composition of the compound was well determined: a majority bixbyite phase (86 mol%, 94 wt%) with $(Fe_{0.25}Mn_{0.75})_2O_3$ stoichiometry and average crystallite size of ~48 nm, plus a minority hematite phase (14 mol %, i.e., 6 wt%) with an average crystallite size of ~8 nm.
- Regarding the Mössbauer spectrum at 80 K, the area ratio between the 24d and 8b crystallographic sites and the percentage areas of the two doublets were used as constraints in the Rietveld analysis of the x-ray diffraction (XRD) data. These combined techniques (Mössbauer + Rietveld refining) have been uses to precisely determine the stoichiometry for $(Fe_xMn_{1-x})_2O_3$, i.e. $x = 0.25$.
- Raman spectroscopy confirmed the presence of characteristic vibrational bands, supporting the identification of the majority phase. X-ray photoelectron spectroscopy analysis detected oxygen vacancies on the $(Fe_{0.25}Mn_{0.75})_2O_3$ particle surface with varying oxidation states (Fe^{3+}, Fe^{2+}, Mn^{3+}, and Mn^{4+}). X-band magnetic resonance data exhibited a strong and broad resonance line throughout the temperature range (4.3 K $\leq$ T $\leq$ 300 K), primarily governed by the majority phase.
- The temperature dependence of both resonance field and resonance linewidth shows a remarkable change in the range of 40–50 K, herein credited to surface spin glass behavior. The model picture used to explain the MR data in the lower temperature range (below about 50 K) assumes $(Fe_xMn_{1-x})_2O_3$ nanoparticles with a core-shell structure. These results indicate that below about 50 K the shell's spin system reveals a paramagnetic to spin glass-like transition upon cooling, with a critical temperature estimated at 43 $\pm$ 1 K. In the higher temperature range, the superparamagnetic hematite (secondary) phase contributes remarkably to the temperature dependence of the resonance linewidth. Zero-field-cooled (ZFC) and field-cooled (FC) data show strong irreversibility and a peak in the ZFC curve at ~33 K, attributed to a paramagnetic-ferrimagnetic transition of the main phase.
- Hysteresis curve at 5 K shows a low coercive field of 4 kOe, with the magnetization not reaching saturation at 70 kOe, suggesting the occurrence of a ferrimagnetic core with a magnetic disorder at surface, characteristic of core-shell spin-glass-like behavior.

GRAPHICAL ABSTRACT

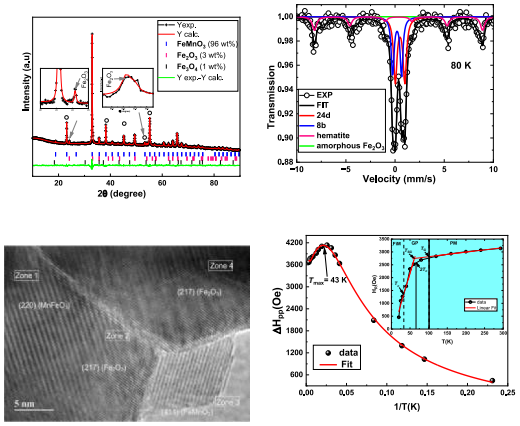

ARTICLE INFO

Keywords:
$FeMnO_3$
$(Fe_xMn_{1-x})_2O_3$
Sol-gel method
Magnetic nanoparticles
Magnetic phase transition
Mössbauer spectroscopy
Magnetic resonance

ABSTRACT

This report aims to investigate in depth $FeMnO_3$, a material of interest due to its fascinating magnetic and multiferroic properties and its many applications in fields including lithium-ion batteries, microwave devices, and catalysis. However, understanding the precise stoichiometry of the material is crucial for a better comprehension of its physical properties. A cheap, simple, and repeatable sol-gel process was used to fabricate the $FeMnO_3$ nanocrystals. Comprehensive multi-technique characterization of the as-fabricated $FeMnO_3$ indicates that the main phase (94 wt%) is $Fe_{0.5}Mn_{1.5}O_3$, although hematite appears as the minority phase (6 wt%). Magnetic characterization shows core-shell spin-glass like behavior, as well as paramagnetic-ferrimagnetic transitions and a Griffiths phase regime. EPR measurements revealed a strong and broad resonance line across the temperature range of 4.3 K–300 K, primarily influenced by the majority phase. The g-value decreases monotonically from 2.93 at 50 K to 2.18 at 300 K. There is a notable change in the resonance field and linewidth between 40 and 50 K, attributed to surface spin glass behavior. The EPR data below 50 K are in line with the core-shell model of $(Fe_{0.25}Mn_{0.75})_2O_3$ nanoparticles. Below 50 K, the shell's spin system undergoes a transition from paramagnetic to spin-glass-like, with a critical temperature around 43 K. Above 50 K, the superparamagnetic minority phase significantly affects the temperature dependence of the resonance linewidth. These results hold particular importance as they advance our understanding of the intricate magnetic interactions present in $FeMnO_3$. For the best possible use of this material platform in new technologies, such insights are essential.

1. Introduction

Nanotechnology has engendered a paradigm shift across various domains of science and technology, empowering manipulation and governance of matter at the nanoscale. The extraordinary and distinct properties of nanomaterials have ushered in novel prospects for applications in medicine, electronics, energy, and a plethora of other fields. Moreover, nanotechnology has yielded substantial progress in the fabrication of more efficient and miniaturized devices, fostering a world that is increasingly interconnected and technologically sophisticated. Given its capacity to tackle intricate challenges and enhance the quality of life, nanotechnology continues to stand as a captivating and auspicious arena for research and development endeavors. Nanostructured magnetic semiconductors, including mixed metal oxides, hold particular interest for technological applications due to the versatile nature of their physical and chemical properties, derived from both stoichiometry and particle size. As widely acknowledged, these properties often differ from those observed in the same materials but with micrometric and larger particle sizes. Among the wide variety of nanomaterials available, such as ferrites, hexaferrites and magnetites, each suitable for specific applications, for example hexaferrites stand out due to several distinct advantages. Unlike metals, alloys and composites, which suffer significant losses due to eddy currents, hexaferrites exhibit superior microwave properties and exceptional stability under extreme conditions, as reported in the literature [1,2]. On the other hand, manganites, which are perovskite oxides with the general formula $R_{1-x}M_xMnO_3$, where R is normally a trivalent rare-earth ion and M is usually a transition metal or a divalent alkaline ion, are widely recognized for exhibiting intriguing properties [3]. Materials from the $R_{1-x}M_xMnO_3$ family, especially when the particle size is in the nanometer range, can exhibit remarkable densities of ionic and electronic defects, making them important candidates for the development of solid-state fuel cells, chemical gas sensors, magnetic refrigeration, and eventually as memory storage devices [4,5]. Just as in all perovskites, the composition, oxygen stoichiometry and structural parameters strongly influence the physico-chemical properties of manganites [5–8]. On the other hand, it is well established that the fundamental state of a given manganite can be modified by variations in basic thermodynamic variables such as pressure and strain, as well as by the application of electric and magnetic fields [9–11].

An interesting aspect of these nanocomposites prepared by several techniques is the occasional presence of a secondary phase (or adding a new phase purposely), which can produce a synergistic effect in bi-phase systems. This is particularly intriguing because it can enhance the physical properties such as the magnetic properties, as reported by Trukhanov et al. [12], additionally, combining various polymers with oxide compounds results in new promising composite materials, as demonstrated in the literature [13]. The basic building block of manganites with a perovskite structure is the MnO_6 octahedron. According to Travis et al. [14], a compound from the manganite family will exhibit a stable perovskite structure when the Goldschmidt tolerance factor t is within the range of $0.89 < t < 1.02$. Considering a particular magnetite with composition $AMnO_3$ (where A represents a rare-earth ion or a transition metal ion), the Goldschmidt tolerance factor is defined as follows [15]:

$$t = \frac{1}{\sqrt{2}} \frac{r_A + r_O}{(r_{Mn} + r_O)}$$

being r_A (r_{Mn}) the ionic radius of the A^+ (Mn^+) cation and r_O the ionic radius of the O^- anion. Note that $t = 1$ corresponds to the ideal perovskite structure [15]. The perovskite lattice undergoes structural deformation primarily due to two types of distortions: one results from the tilting of the MnO_6 octahedron, whereas the other arises from the asymmetry in the six Mn–O bond lengths surrounding the Mn atom within the MnO_6 octahedron (the Jahn-Teller distortion [16]). Moreover, impurities such as interstitial oxygen atoms, can significantly impact the structural deformation of the perovskite crystal lattice, leading to changes in the Mn oxidation state and affecting the overall charge balance and structural stability. Simultaneously, there has been a remarkable surge in interest towards investigating non-perovskite structures of the ABO_3 type (where A and B represent cations such as Co, Ni, Fe, Mn, etc.). This heightened interest can be attributed to their multifunctional properties and promising potential for diverse device applications [17,18].

Notably, manganese oxide, in which manganese can exist in various valence states, has garnered extensive attention due to its intriguing magnetic and multiferroic characteristics [19–21]. Furthermore, altering the composition results in concurrent changes in structure and valence states. For instance, in the case of MnO, which adopts a halite-type cubic structure, the Mn ion exhibits a valence state of 2+. In contrast, for Mn_2O_3, with a bixbyite structure (either cubic or orthorhombic), the valence state is 3+. Similarly, in Mn_3O_4, possessing a spinel cubic structure, the Mn ion displays a mixed valence of 2+ and 3+ [22].

Remarkably, different classes of complex iron oxides have excellent electronic properties such as ferrites [23], and $AMnO_3$-type compounds. Regarding the latter, bixbyite compound $FeMnO_3$, have found versatile applications, such as in negative temperature coefficient (NTC)

thermistors, oxidation catalysis, and superparamagnetic materials. Cao et al. [24] extensively investigated $FeMnO_3$ as an anode material for lithium-ion batteries. This compound has gained prominence in electrochemistry owing to its intriguing redox behavior, superior theoretical capacity for lithium-ion batteries (500–1000 mAh/g), and lower operating potential [25]. Furthermore, $FeMnO_3$ has been effectively employed in microwave devices and catalysts. The bixbyite-based (Mn^{3+}, Fe^{3+})$_2O_3$ compound adopts the β-Mn_2O_3 crystal structure (cubic, *Ia-3*, $a = 9.41$ Å) [21]. It comprises two metal sites situated at the 24d and 8b crystallographic positions, whereas the oxygens occupy the 48e positions [26].

Both cations exhibit octahedral coordination with oxygen, with the 8b site displaying a slight trigonal distortion, whereas the 24d site exhibits a more substantial distortion. Rayaprol et al. [27,28] conducted a thorough investigation of the magnetic and magnetocaloric properties of $FeMnO_3$ synthesized through mechano-synthesis. It would be anticipated that Fe^{3+} and Mn^{3+} ions, in octahedral coordination with oxygen, would possess high-spin configurations with quenched orbital moments, leading to magnetic moments of 5.9 μ_B (Fe^{3+}) and 4.9 μ_B (Mn^{3+}), resulting in an expected average of 5.5 μ_B per metal site. Through fitting the magnetization data in the 200–380 K range using the Curie-Weiss law, the authors previously derived an average magnetic moment per site of 4.1 μ_B, suggesting the presence of some degree of antiferromagnetic correlation even at higher temperatures [29].

Various preparation techniques have been successfully employed to synthesize nanosized $FeMnO_3$, including physical methods such as high-energy ball milling, as well as chemical techniques like chemical co-precipitation, sol-gel, combustion, and sputtering [30–33]. The physical and chemical attributes of the materials produced through the sol-gel approach, such as particle size, surface area, and mechanical properties, can exhibit significant variations depending on factors such as working temperature, operating conditions, and chemical precursors utilized. However, it has been documented that the sol-gel method offers a highly reproducible means of fabricating nanomaterials with elevated surface area and improved mechanical properties when compared to alternative synthetic routes [34]. Nonetheless, it is noteworthy that a limitation of the sol-gel method lies in the sensitivity of the precursor's hydrolysis to water addition. Even under vigorous stirring, the rate of hydrolysis is so rapid that particles tend to precipitate immediately upon water introduction into the reaction medium. A reduced rate of hydrolysis, however, can result in particle size reduction and an increase in surface area, aspects of great interest in catalysis [35]. The stability of various compounds formed within the $FeMnO_3$ system is contingent not only on the Fe/Mn/O ratios but also on the preparation method and calcination temperature [36]. Among the identified compounds are mixed oxides $(Fe_{1-x}Mn_x)_{1-y}O$, which have been utilized in water-splitting reactions [36], rock-salt oxides $Fe_xMn_{1-x}O$ [37], defect spinel γ-$FeMnO_3$ analogous to γ-Fe_2O_3 [38], and manganese-substituted magnetite $Mn_xFe_{3-x}O_4$ [39]. In a study conducted by Ponce et al. [40], it was revealed that the stability of Mn^{4+} ions play a critical role in determining the catalytic activity of manganites for methane oxidation in the temperature range of 200–800 °C. Generally, high surface area is associated with small particle sizes, leading to a larger surface area exposed to gases for a given mass of nanoparticles [41,42]. Considering the $FeMnO_3$ compound as paradigmatic for this family, there are few studies that have explored the physical and morphological characteristics of compounds with excess or deficiency of Fe, with the exception of the first-principles study by Bazhenova and Honkala [43].

In this investigation, we present a comprehensive exploration of the physical properties exhibited by $Fe_{0.5}Mn_{1.5}O_3$ nanoparticles synthesized using the sol-gel method. A meticulous evaluation of the structural, morphological, optical, and magnetic characteristics was undertaken through a combination of cutting-edge techniques, including x-ray diffraction (XRD), x-ray photoelectron spectroscopy (XPS), transmission electron microscopy (TEM), Raman spectroscopy, Mössbauer spectroscopy (MS), magnetometry, and electron magnetic resonance (EMR).

The proficient integration of MS, XPS and XRD techniques, the latter skillfully resolved through Rietveld analysis, enabled a meticulous elucidation of the system's precise stoichiometry. Additionally, this approach facilitated the unequivocal identification of the distinct phases present in the sample, their corresponding fractions, and the mean sizes of their crystallites. The magnetic properties of the compound were exhaustively characterized using the aforementioned techniques, and the results were effectively correlated with the morphology and composition of the studied material.

2. Experimental details

2.1. Sample preparation

The $(Fe_{0.25}Mn_{0.75})_2O_3$ nanoparticles (NPs) reported here were synthesized using sol-gel polymerization method, which utilized transition metal nitrates as precursors [6]. The process involved dissolve manganese nitrate tetrahydrate ($Mn(NO_3)_2{\cdot}4H_2O$) (99 %), ferric nitrate nonahydrate ($Fe(NO_3)_3{\cdot}9H_2O$) (Aldrich 99.95) and citric acid ($C_6H_8O_7$) in a small quantity of double distilled water. Aqueous solutions of manganese (0.4 mol/L) and iron (0.8 mol/L) nitrates were mixed in stoichiometric proportion (Fe^{3+}:Mn^{2+}1:1). The mixture was then diluted in 50 mL of ethylene glycol (99 % purity) while keeping the 1:1 vol ratio. The homogeneous reaction medium was stirred at 80 °C to ensure uniformity. Once the gel was formed the temperature was raised to 250 °C for self-ignition reaction. The resulting product was subsequently calcined under ambient atmosphere (900 °C, 72 h) to obtain the nanosized compound.

2.2. Characterization details

Structural analysis of the as-synthesized powder at room temperature were performed using a commercial XRD diffractometer (Rigaku, model D/max) equipped with copper radiation source Cu-$K\alpha$ (λ = 1.5418 Å) and operating in steps (2θ) of 0.05°. Crystal structures were refined using the Rietveld method [44] with GSASII suite program [45]. Representative TEM micrographs of the sample, including energy dispersive x-ray spectroscopy (EDX), were obtained using a commercial microscope (JEOL, model JEM-2100). Raman spectra were recorded using a triple spectrometer (Jobin-Yvon, model T64000) equipped with a 2048 × 512 pixels nitrogen-cooled CCD (Charge-Coupled Device) camera. Compositional XPS analysis was performed on a Specs surface analysis system equipped with a Phoibos 150 electron analyzer using a monochromatized Al Kα radiation (1486.6 eV) at a power of 350 W. Casa XPS software was used to process the recorded data and to estimate the sample surface atomic concentration. C -1s signal (284.6 eV) was used as reference for calibration of the binding energies (BE) of different elements. Electron magnetic resonance (EMR) spectra (from 3.8 to 300 K) were collected using a commercial X-band spectrometer (Bruker, model EMX) equipped with a rectangular cavity. ^{57}Fe Mössbauer spectra in transmission mode were recorded at 80 K and 300 K using a conventional spectrometer. The sample was mixed with boron nitrate (reaching 0.1 mg ^{57}Fe per cm^2) and homogeneously dispersed within a nylon-based sample holder. The spectrometer was equipped with a 25 mCi ^{57}Co source, immersed in Rh matrix. The Mössbauer source was coupled to the driver (room temperature) while a sinusoidal velocity driver was used. A cryostat (Oxford Cryosystems) equipped with a temperature controller was able to keep the sample in the desirable temperature. The dc magnetic measurements were performed using a commercial SQUID (MPMS, Quantum Design) magnetometer varying the temperature in the range of 5–300 K while applying magnetic fields up to ± 70 kOe.

3. Results and discussion

3.1. Mössbauer spectroscopy

The Mössbauer spectra recorded at 295 K and 80 K and their fits, including the subspectra (colored solid lines), are shown in Fig. 1a and b, respectively. These fits were performed using two doublets corresponding to 24d and 8b crystallographic positions of the $(Fe,Mn)_2O_3$ phase, plus two sextets identified as hematite (α-Fe_2O_3), and amorphous hematite. The obtained hyperfine parameters are collected in Table 1.

The Mössbauer sextet (1) is assigned to crystalline α-Fe_2O_3 in a weakly ferromagnetic-like spin state for both temperatures, as suggested by the quadrupole splitting values of $\Delta = -0.21$ mm/s at $T = 295$ K and $\Delta = -0.17$ mm/s at $T = 80$ K, typical of this magnetic ordering [46]. Therefore, no Morin transition (T_M) is expected in the range of 295 - 80 K. Moreover, according to Amin and Arajs [47] $T_M = 264.2–2194/d$, where d is the nanoparticle diameter (in nm) and T_M is the Morin temperature (in K units). Then, using the lower temperature value ($T_M = 80$ K), one can estimate the mean size of the as-synthesized α-Fe_2O_3 nanoparticles below 12 nm. This result agrees with the mean size estimated by XRD analysis (8 nm). According to the literature, the Morin temperature decreases as the mean particle size decreases, tending to be quenched for particles smaller than about 8 nm in mean size [47,48]. Negative values of quadrupole splitting are also found for sextet (2), indicating weakly ferromagnetic coupling for this component, at both temperatures (80 and 295 K). Bulk hematite is a weak ferromagnet below the Néel temperature (948 K $\leq T_N \leq$ 963 K) which undergoes a magnetic phase transition (to antiferromagnet and presenting spin reorientation) at the Morin temperature ($T_M \approx 263$ K). For the doublets, as can be seen in Table 1, the low temperature (80 K) isomer shift (δ) and quadrupole splitting (Δ) of 24d site, are 0.61 mm/s and 0.96 mm/s, respectively, which are higher than the 0.31 mm/s and 0.90 mm/s found for the 8b site. The larger values of both Δ and δ, obtained for 24d site, agree well with the values reported by Nell et al. [49] in natural and synthetic samples of $FeMnO_3$. However, the Δ values for both sites are significantly higher than the values reported at room temperature in other studies [39,49]. This is likely related to the preparation method of the samples used here, which results in more distorted nanocrystals than those reported in the literature. The area ratio of the doublets, $Area_{24d}/Area_{8b} = 1.79$ was extracted at 80 K. This value, equivalent to the ratio of the iron populations of these sites, will be used as a constraint for the Rietveld analysis. For the Mössbauer sextet (2), the unusual large linewidth value ($\Gamma = 0.87$ mm/s, $T = 80$ K) obtained for the amorphous hematite confirms the degree of amorphization, with the decrease of the hyperfine field, as compared to the crystalline hematite (see Table 1). Moreover, Kolk et al. [50] studying hematite nanoparticles have also reported the presence of an additional component with broader linewidth and hyperfine field of about 480 kG, which was attributed to amorphous α-Fe_2O_3, whereas the crystalline hematite showed hyperfine field of 525 kG at 15 K.

Table 1
List of hyperfine parameters obtained from the fits of the Mössbauer spectra, where $\delta$is the isomer shift, Δ is the quadrupole splitting, Γ is the linewidth, Area is the percentage area of the corresponding subspectrum, and B_{hf} is the hyperfine field. $\delta$is given relative to α−Fe.

T (K)	Subspectrum	δ (mm s^{-1})	Δ (mm s^{-1})	Γ (mm s^{-1})	Area (%)	B_{hf} (kG)
80	Doublet (1), 24d	0.61(1)	0.96(1)	0.42(1)	41(2)	–
	Doublet (2), 8b	0.31(1)	0.91(1)	0.33(1)	23(2)	–
	Sextet (1)	0.47(2)	−0.17(2)	0.48(2)	25(2)	528 (2)
	Sextet (2)	0.55(2)	−0.09(2)	0.87(2)	11(2)	482 (2)
295	Doublet (1), 24d	0.49(1)	0.95(1)	0.43(1)	45(2)	–
	Doublet (2), 8b	0.18(1)	0.90(1)	0.33(1)	25(2)	–
	Sextet (1)	0.39(2)	−0.21(2)	0.33(2)	16(2)	508 (2)
	Sextet (2)	0.38(2)	−0.18(2)	1.27(2)	14(2)	473 (2)

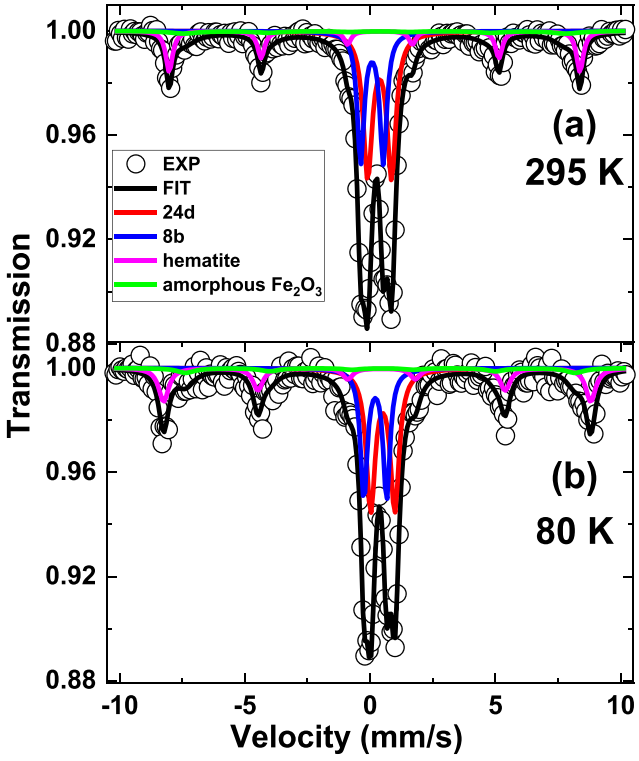

Fig. 1. Fittings of ^{57}Fe Mössbauer spectra of the as-synthesized sample measured at 295 K and 80 K. The open circles represent experimental data whereas the solid lines represent curve fittings. One doublet represents Fe^{3+} occupying 24d sites (solid red line) and the other doublet represents Fe^{3+} occupying 8b sites (solid blue line). The sextets are assigned to crystalline (solid magenta line) and amorphous (solid green line) hematite.

3.2. X-ray diffraction

Fig. 2 shows the room-temperature XRD pattern of the as-prepared powder sample. The XRD data was refined using the Rietveld refinement method (GSASII software). The refinement analysis indicated formation of a cubic structure, space group Ia-3, bixbyite $(Fe^{3+}Mn^{3+})O_3$

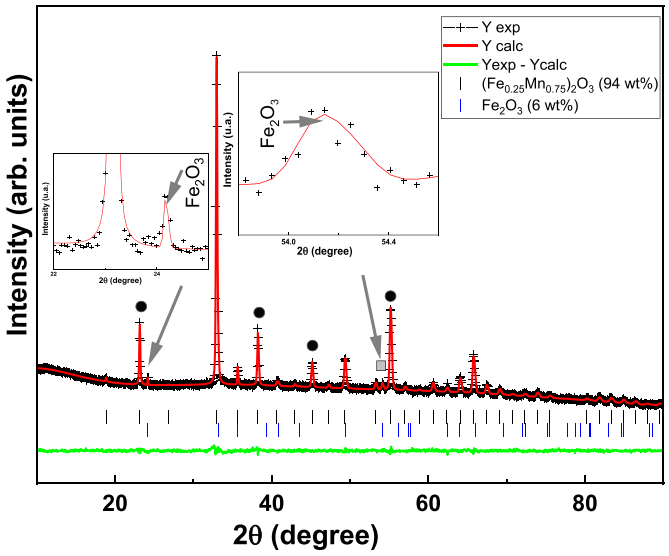

Fig. 2. Room temperature XRD pattern of the as-synthesized sample, with the calculated data represented by the solid red line and black symbols indicating experimental data. The solid green line at the bottom shows the difference between the experimental (Yexp) and calculated (Ycalc) data. Bragg's reflections of the standard $(Fe_{0.25}Mn_{0.75})_2O_3$ and α-Fe_2O_3 phases are indicated by vertical black and blue ticks, respectively.

type structure as the majority phase (~86 mol%), and another minority phase identified as hematite (~14 mol%) as shown in Fig. 2. The parameters obtained from the refinement are listed in Table 2.

The fractional positions for the bixbyite phase as well as the fitting parameters of the α-Fe_2O_3 phase are included in Table 2. A lattice constant of $a = 9.412(1)$ Å corresponding to the bixbyite phase was found, which is consistent with the value reported in the literature (9.41 ± 0.03) Å for the $FeMnO_3$ formed in the bixbyite phase and prepared via mechanosynthesis [28].

The stoichiometry $(Fe_{0.25}Mn_{0.75})_2O_3$ was deduced from the Fe and Mn occupancies (see Table 2).

In agreement with the results obtained from MS, it was verified that the Fe atoms site occupancy ratio (24d/8b) is 1.79. It was also possible to calculate the ratio of Fe atoms in the $(Fe_{0.25}Mn_{0.75})_2O_3$ phase with respect the total amount of Fe atoms (all phases), resulting in (0.61 ± 0.02). This finding is also in agreement with the result obtained from MS, considering the uncertainties, and allows one to conclude that this is the most reliable stoichiometry for the as-synthesized sample.

The mean crystallite size ($<L_{XRD}>$) of the $(Fe_{0.25}Mn_{0.75})_2O_3$ phase was estimated using the modified Scherrer's equation. This was accomplished while plotting $\ln\delta$ versus $\ln(1/\cos\theta)$ to obtain the y-axis intercept $\ln(k\lambda/<L_{XRD}>)$, using least square linear regression, where k is a constant (0.89 for spherical nanoparticle), λ is the wavelength of the x-ray (Cu-$K\alpha$), δ is the full width at half maximum (FWHM) of the x-ray diffraction line, and θ is the corresponding diffraction angle [52]. The mean crystallite size $<L_{XRD}>$ ~48 nm was estimated for the $FeMnO_3$ phase using the (211), (400), (332) and (440) Bragg planes (see solid black circles in Fig. 2). To estimate the mean crystallite size of the secondary α-Fe_2O_3 phase, the Scherrer's equation was used only for the (116) plane (see the square gray in Fig. 2), once it represents the highest XRD intensity peak observed for this phase. Then, $<L_{XRD}>$ ~8.0 nm was estimated for the α-Fe_2O_3 phase.

3.3. Morphology

Fig. 3a shows a representative TEM micrograph of the $FeMnO_3$ like sample produced at 900 °C. As see in Fig. 3a and b, irregularly shaped particles with a wide range of sizes extending from 20 to 820 nm are observed. The crystal structure of the $(Fe_{0.25}Mn_{0.75})_2O_3$ was also examined by selected-area electron diffraction (SAED). The selected area electron diffraction (SAED) pattern, obtained from the $(Fe_{0.25}Mn_{0.75})_2O_3$ sample (highlighted by the white circle in Fig. 3b), reveals a distinctive arrangement of broad concentric diffraction rings. Notably, the rings correspond to crystallographic planes such as (200), (211), (321), (222), (411), and (422), attributing them to the cubic phase of the $(Fe_{0.25}Mn_{0.75})_2O_3$ sample (depicted in Fig. 3d) [53]. Remarkably, the absence of the hematite phase in this SAED pattern suggests that it does not coat the particle surface. Instead, a secondary phase is formed. This intriguing observation is underscored by the clear absence of the aforementioned electron diffraction associated with hematite in this particular region. The crystallographic planes of each diffraction ring are explicitly indicated in Fig. 3d.

The EDX spectrum recorded from the as-synthesized sample is shown in Fig. 3e. As observed, the peaks corresponding to Mn, Fe and O confirm the presence of these elements in the major phase $(Fe_{0.25}Mn_{0.75})_2O_3$. The C and Cu signal appearing in the EDX spectrum is due to the tape and grid used for sample preparation, respectively.

3.4. Raman spectroscopy

The crystallographic symmetry is the bixbyite structural type with the *Ia-3* space group having 22 Raman active modes described by: $4A_g + 4E_g + 14F_g$ [54], 10 inactive modes $5A_u + 5E_u$, and 16 T_u IR modes [53]. Despite the large number of Raman active modes (22), the number of modes actually observed in the Raman spectrum is reduced [54]. Fig. 4 shows the room-temperature Raman spectrum of the as-synthesized powder sample in the 200-800 cm^{-1} range. According to the

Table 2
Structural and statistical parameters obtained from the Rietveld refinement of x-ray diffraction. V is the cell volume, GOF is the goodness of fit and χ^2 is the chi-square quality parameter. $x^2 = 1.69$; GOF = 1.30.

	a (Å)	b (Å)	c (Å)	V(Å)^3	Space group	Phase percentage (mol%)
$(Fe_{0.25}Mn_{0.75})_2O_3$	9.412(1)	9.412(1)	9.412(1)	833.818(1)	Ia-3	86(1)
α-Fe_2O_3	5.036(1)	5.036(1)	13.730(2)	301.514(1)	R-3c	14(1)
Fractional positions of $(Fe_{0.25}Mn_{0.75})_2O_3$						
Atom	Wyckoff Position	x	y	z	Occupancy	
Fe_1	8b	0.2500(2)	0.2500(2)	0.2500(2)	0.356	
Mn_1	8b	0.2500(2)	0.2500(2)	0.2500(2)	0.644	
Fe_2	24d	0.0308(2)	0.0000	0.2500(2)	0.212	
Mn_2	24d	0.0353(2)	0.0000	0.2500(2)	0.788	
O	48e	0.3342(2)	0.1048(2)	0.1196(2)	1.0000	
Fractional positions of Fe_2O_3						
Fe	12	0.0000	0.0000	0.3544(3)	1.0000	
O	18	0.3723(2)	0.0000	0.2500(2)	1.0000	

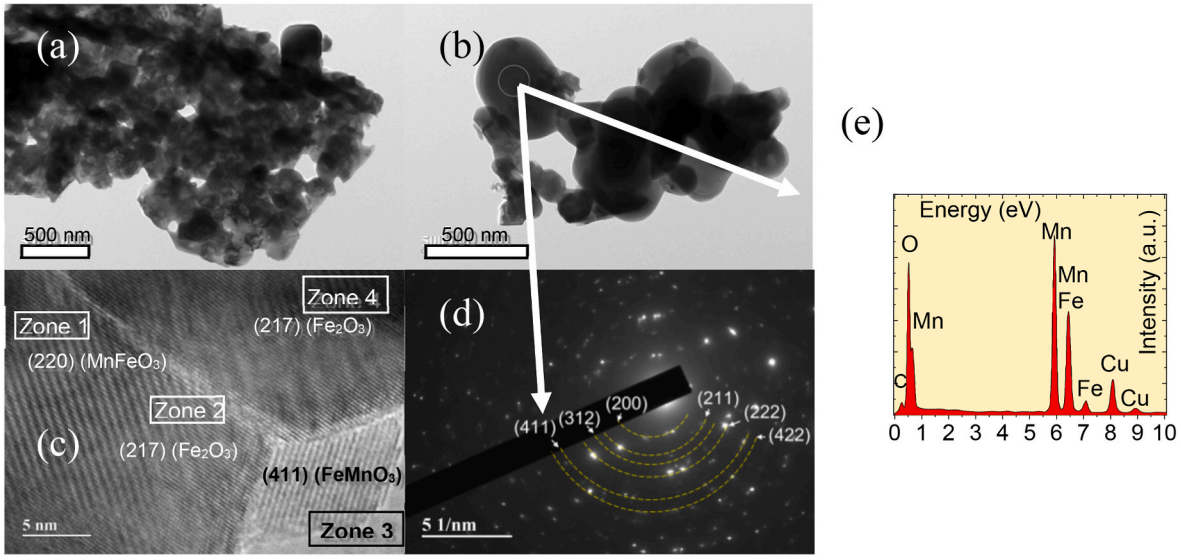

Fig. 3. (a) and (b) TEM images of the as-synthesized sample (scale bar in nm). (c) HRTEM image of the as-synthesized sample with Zone 1 and Zone 3 referring to interplanar distance of the $FeMnO_3$ phase, whereas Zone 2 and Zone 4 refer to the α-Fe_2O_3 phase (scale bar in nm). (d) SAED pattern for the as-synthesized sample (scale bar in nm). (e) Shows the EDX spectrum of the as-synthesized sample recorded in the indicated position (white circle) of panel (b).

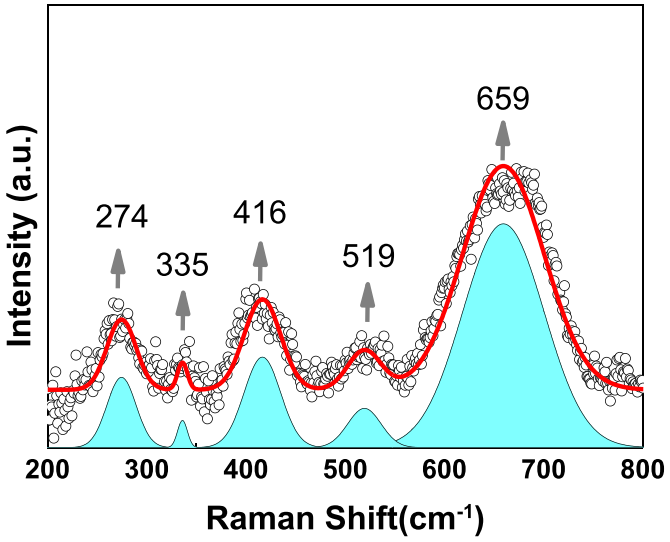

Fig. 4. Raman spectrum of the as-synthesized sample. The experimental data are represented by open black symbols whereas the solid red line portrays the best fitting obtained by incorporating blue colored components.

above-mentioned crystallographic symmetry, the bixbyite structural type is the source of the Raman active modes in the spectrum, which is consistent with the XRD result. Furthermore, the bands exhibit broadness, which is unexpected given the higher average particle size reported by XRD and TEM. Concurrently, this implies a significant degree of disorder, particularly at the particle surface, as the Raman shows a greater surface contribution than the XRD.

The characteristic vibrational bands observed at 659 cm^{-1}, 519 cm^{-1} and 416 cm^{-1} correspond to three of 14 F_g modes which are labeled as $F_g^{(1)}$, $F_g^{(2)}$, and, $F_g^{(3)}$, respectively. The band located at 335 cm^{-1} is assigned to the $E_g + F_g$ mode, meanwhile, the 274 cm^{-1} band is linked to the E_g mode. To display the effect of the presence of iron in the bixbyite holding matrix we can highlight the spectrum reported by Chen et al. [55] which displays the $F_g^{(1)}$ located at 652 cm^{-1} linked to the Mn^{3+}-O mode vibration. When iron is present in the Mn/FeO_6 octahedral, as in the case of the $FeMnO_3$, vibrations can cause the Raman frequencies to shift to lower values; these downshift being also observed in the $F_g^{(2)}$ and $F_g^{(3)}$ vibrational modes [55].

3.5. Surface composition analysis

XPS measurements were performed to examine the oxidation state of Fe and Mn and the presence of oxygen specimens on the surface of the nanoparticles. The background was modeled using a Shirley-type function implemented in Casa XPS software, and all positions were corrected using the expected 284.6 eV position of the C 1s binding energy.

The high-resolution spectrum of Fe 2p, displayed in Fig. 5a, clearly shows Fe $2p_{1/2}$ and Fe $2p_{3/2}$ enlarged photoelectron lines (PL), suggesting that there are two sets of peaks corresponding to two different oxidation states. In this regard, a good fit was obtained using two PL for each Fe 2p peak, deconvoluted into two mixed Gaussian-Lorentzian-shaped peaks. The doublets binding energies (BEs) obtained have been located at 710.2 eV/723.6 eV, and 712.5 eV/725.9 eV, which were assigned to Fe^{2+} and Fe^{3+} oxidation states, respectively. In addition, satellite peaks were observed at 715.1 eV/719.7 eV and 728.3 eV/733.3 eV which are also characteristic of Fe^{2+} and Fe^{3+}, respectively [56]. The percentage of each species was estimated from the integrated areas of each peak to be around ~43 % of Fe^{3+} and ~57 % of Fe^{2+}. These values are consistent with the crystalline state identified with different occupational sites for Fe atoms using XRD and MS.

As shown in Fig. 5b, the fitting of the Mn 2p core level high-resolution XPS spectra reveals two component features as well, which are centered at 641.0eV/643.1eV and 652.4 eV/654.2 eV. The Mn $2p_{3/2}$ and Mn $2p_{1/2}$ features centered respectively at binding energies ~641.0eV and ~652.4 eV, are indication of the presence of Mn^{3+} ions with a spin-orbit split equals to ~11.4 eV. Moreover, the binding energies ~643.1 eV and 654.2 eV are indication of presence of presence of Mn^{4+} ions with a spin-orbit split equals to ~11.1 eV. The satellites of the Mn $2p_{1/2}$ peak are located at 663.3 eV and 667.4 eV, with a separation between them of about 9 eV (see Fig. 5b), which is a fingerprint of the Mn^{3+} and Mn^{4+} oxidized state, respectively [57]. The XPS spectrum of O 1s, revealing three peaks, with binding energies of approximately 529.9, 531.3 and 533.0 eV, present integrated areas of 34 %, 45 % and 20 %, respectively. Similar observation is reported in $BaTiO_3$ [58], which has been assigned to O^{2-} ions, O^{1-} ions, and O^{Chem} species. Regarding the high percentage of O^{Chem} species observed (20 %) it could be associated with oxygen vacancies present on the surface of the $FeMnO_3$

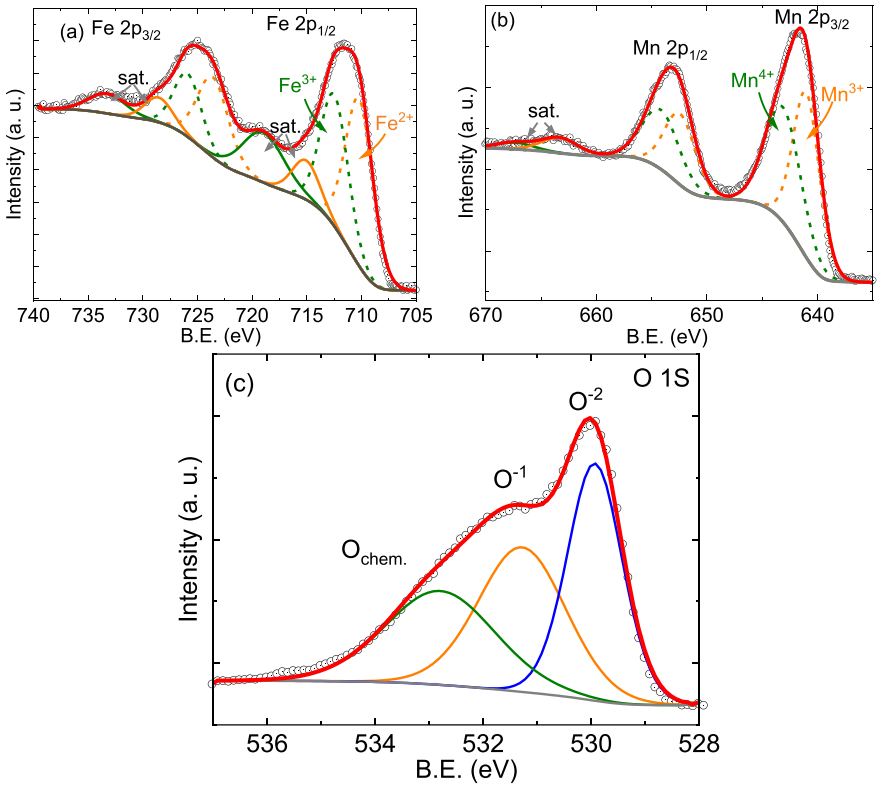

Fig. 5. XPS spectra of the as-synthesized sample, with panels (a), (b), and (c) representing the high-resolution XPS spectra of Fe 2p, Mn 2p, and O 1s, respectively.

nanocrystals. The presence of oxygen vacancies (V_O) can induce changes in the oxidation states of transition metals, such as Mn and Fe, as the system attempts to achieve charge neutrality. Specifically, the presence of V_O can result in coexistence of different oxidation states, such as Mn^{3+}/Mn^{4+} or Fe^{2+}/Fe^{3+} (as evidenced by the recorded XPS data). Such coexistence can introduce mixed valence superexchange interactions that may significantly affect the magnetic properties [2,59]. It is worth noting that this technique can detect only oxides at the surface (up to 2 nm deep into the nanoparticle). The core of the nanoparticles may have different composition, very likely prevailing the oxide with Fe^{3+} and Mn^{3+}.

3.6. Magnetic measurements

Fig. 6a and b shows the magnetization hysteresis loop for the as-synthesized sample at 300 K and 5 K, respectively. The magnetization at 300 K is consistent with the presence of mainly a paramagnetic behavior, superimposed to superparamagnetic response, the latter saturating at relatively small magnetic field. The dashed line in Fig. 6a indicates the saturation magnetization of the superparamagnetic contribution credited to the α-Fe_2O_3 secondary phase [60,61] according to the percentage of phases listed in Table 2. The inset in Fig. 6a shows the central part of the 300 K M vs H curve (magnetic field up to ± 10 kOe). Therefore, the magnetization data confirm the presence of α-Fe_2O_3 secondary phase as determined from the Rietveld refinement data analysis. Moreover, the negligible value for the coercive field at 300 K confirms the superparamagnetic regime for these phases [62].

It is worth noting that the particles of the hematite phase have been determined as blocked at 300 K, once the Mössbauer spectra for them are two magnetic sextets.

This disagreement is due to different time of measurements involved for the magnetization (10^2 s) and Mössbauer spectroscopy (10^{-8} s) techniques, resulting in higher T_B for the latter (MS). While comparing Fig. 6a and b, one finds remarkable differences between the M vs H curves collected at 300 K and 5 K, reflecting the magnetic evolution of the dominant phase. For instance, the coercive field increase, which is discussed in detail in the next paragraphs. The temperature dependence of zero-field-cooled (ZFC) and field-cooled (FC) magnetization curves of the as-synthesized sample obtained with a magnetic field of 20 Oe is shown in Fig. 7. The ZFC curve presents a sharp peak at T_C ~33 K (assigned to the ferrimagnetic transition), following a sharp drop with decreasing T. Simultaneously, a rising feature is observed in the FC curve while decreasing T, showing a strong irreversibility between ZFC and FC curves. This strong irreversibility can be assigned to the presence of the secondary α-Fe_2O_3 phase, besides the majority phase $(Fe_{0.25}Mn_{0.75})_2O_3$. Moreover, the temperature related to the peak observed in the ZFC curve ($T_C \sim 33$ K) is lower than the value reported for the $FeMnO_3$ system prepared by mechano-synthesis ($T_C \sim 40$ K) [28,32]. This is mainly due to samples with different stoichiometry.

To determine the type of magnetic transition involved in the as-synthesized sample, the temperature dependence of the inverse magnetic susceptibility (χ^{-1}) measured at 20 Oe is plotted in Fig. 8.

Data in Fig. 8, regarding the high-temperature range (140–300 K), were fitted (solid red line) to the Curie-Weiss law [63], where:

$$\chi = \frac{M}{H} = \frac{C}{T-\theta} \quad (1)$$

where $C = N\mu_0\mu_{eff}^2/3k_B$ is the Curie constant (N is the number of magnetic ions, μ_0 is the vacuum permittivity, μ_{eff} is the effective magnetic moment per ion, θ is the characteristic Curie-Weiss temperature, and k_B is the Boltzmann constant).

It is worth mentioning that the Curie-Weiss data analysis (see Fig. 8) should reflect both the $(Fe_{0.25}Mn_{0.75})_2O_3$ and α-Fe_2O_3 phases. Moreover, α-Fe_2O_3 nanoparticles should be superparamagnetic in the temperature interval used to fit the data. M. Tadic et al. [64] showed that the FC-ZFC curve is reversible in this interval (101–300K) for their α-Fe_2O_3 nanoparticles with mean crystallite size also equal to 8 nm, and the blocking temperature, T_B = 53K.The best fit provides $\theta = (-177 \pm 2)$ K. The

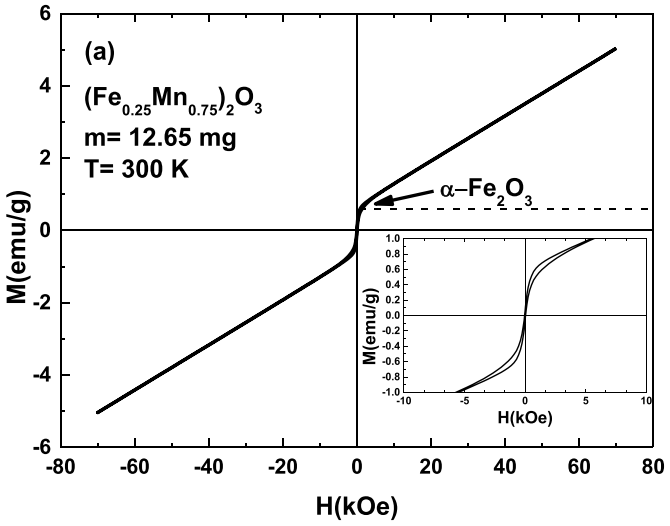

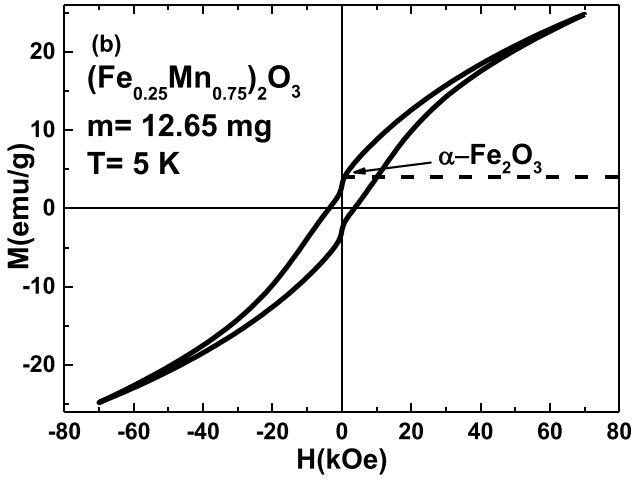

Fig. 6. Magnetization hysteresis loops in the ±70 kOe range obtained (a) at 300 K (the inset shows a zooming of the 300 K plot in the ±10 kOe range) and (b) at 5 K (note the coercivity and magnetic hysteresis in the low field range). Mass of the measured powder is quoted in the legend and the dashed line in panel (a) represents mainly the contribution of the α-Fe_2O_3 (secondary) considering the phase percentage obtained by the Rietveld refining (see Table 2) and the saturation magnetization of bulk α-Fe_2O_3 at 300 K (Ms = 84 emu/cm^3).

negative and relatively high θ value suggests strong AFM interactions between Fe^{3+} and Mn^{3+} magnetic moments in the bixbyite crystallites formed by several unit cells [65]. Moreover, they also indicate the presence of magnetic frustration in the nanocrystals [28]. The literature on $FeMnO_3$ [66] has established the frustration ratio parameter (defined as the ratio between the absolute value of the Curie-Weiss temperature, $|\theta|$, and T_C, i.e. $|\theta|/T_C$) as an indicator of the degree of magnetic frustration in the sample. For our $(Fe_{0.25}Mn_{0.75})_2O_3$ sample, this ratio is $|\theta|/T_C = 177/33 = 5.4$, a value smaller than the one ($|\theta|/\ T_C = 336/32 = 10.5$) obtained by Roth et al. for $(Fe_{0.56}Mn_{0.44})_2O_3$ [66], where a long-range magnetic order was not observed at low temperatures, indicating a prevailing spin glass state. However, our frustration ratio value is higher than the one ($|\theta|/T_C = 69/36 = 1.9$) obtained by Rayaprol et al. [27,28] for $(Fe_{0.5}Mn_{0.5})_2O_3$, in which an antiferromagnetic order is established at low temperature.

A Curie constant of $C = 0.36$ emu/mol × K was obtained from the fit.

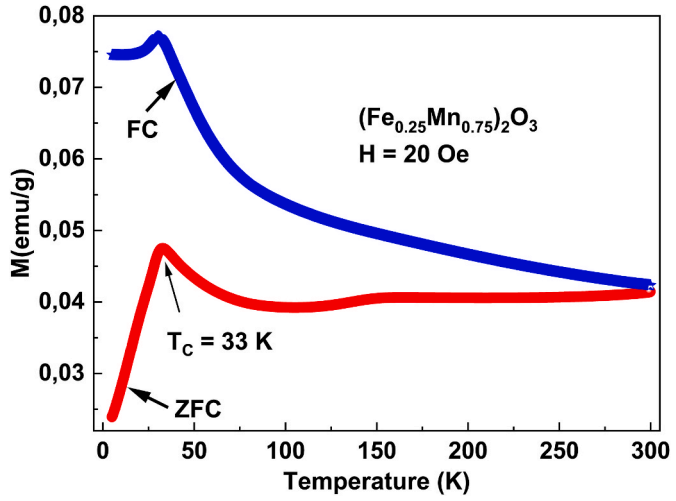

Fig. 7. Temperature dependence of zero-field-cooled (ZFC) and field-cooled (FC) traces obtained while applying a magnetic field of 20 Oe. and the ferrimagnetic transition temperature (T_C).

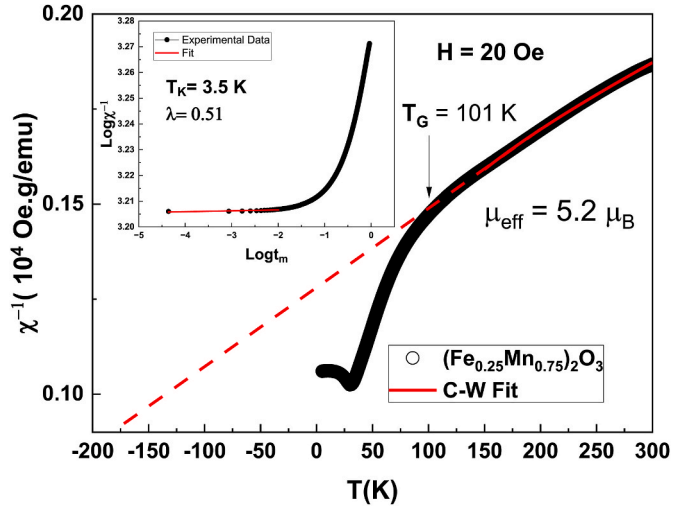

Fig. 8. Temperature dependence of the inverse susceptibility (χ^{-1}), at 20 Oe (black symbols), along with the Curie-Weiss fit (solid red line) in the 150–300 K range using Eq. (1). The inset shows the temperature dependence of the dc susceptibility (following Eq. (2)) plotted in a double logarithmic scale.

From this value, the average magnetic moment of $Fe_{0.5}Mn_{1.5}$ and Fe_1Fe_1 for $(Fe_{0.25}Mn_{0.75})_2O_3$ and α-Fe_2O_3, respectively, is $<\mu_{eff}^{exp}> = 4.8 \pm 0.1\mu_B$. Using the magnetic momentfor2-15nm mesoporous α-Fe_2O_3(=4 $0.05 \pm 0.02\mu_B$) obtained by A. H. Hill et al. [67] at 295 K, as well as the molar fraction of these phases given in Table 2, a value of $\mu_{eff} = 4.92 \pm 0.17\mu_B$ was estimated for $Fe_{0.5}Mn_{1.5}$. This value is higher than the value of 2.8 μ_B determined by Seifu et al. in $FeMnO_3$ compounds produced by the mechanical alloying technique [37]. This is attributed to differences in stoichiometry between the investigated samples Assuming that the electronic configuration of the system is $(Fe^{3+}_{0.5})(Mn^{3+}_{1.5})(O^{2-}_3)$ and taking into account that the theoretical spin-only values are: $\mu^{3+}_{Fe} = 5.90\ \mu_B$ and $\mu^{3+}_{Mn} = 4.90\ \mu_B$ (Fe^{3+} and Mn^{3+} ions in high spin state) [68], the theoretical value of the effective magnetic moment is estimated as: $\mu^{theo}_{eff} = [(1\text{-}f) \times (\mu^{3+}_{Mn})^2 + f \times (\mu^{3+}_{Fe})^2\ ]^{1/2} = 5.2 \pm 0.3\mu_B$, where $f = 0.25 \pm 0.01$ is the percentage of Fe over the total magnetic ions of the system. This result is in agreement with the experimental one considering the uncertainties, confirming that Fe^{3+} and Mn^{3+} ions are in the high spin state configuration.

The downward deviation of the temperature-dependent inverse

magnetic susceptibility (χ^{-1}) from the ideal Curie-Weiss law (see Fig. 8) signals the presence of the Griffiths phase (GP) in the system. The temperature at which $\chi^{-1}(T)$ deviates from the ideal Curie-Weiss law is known as the Griffiths temperature (T_G) herein ascribed to 101 K, as shown in Fig. 8. This feature is a unique characteristic of the GP [69].

A similar downturn was also observed in the antiferromagnetic $TbFe_{0.5}Cr_{0.5}O_3$ and $FeMnO_3$ phases fabricated by the mechanosynthesis method [70], in which the FM correlation among neighboring short-range FM cluster accounts for the observed deviation. Herein, T_G is defined as the onset temperature, where $\chi^{-1}(T)$ data deviates from the Curie-Weiss law, and a local AFM ordered area begins to develop [71]. The GP regime is usually characterized by the temperature dependence of the inverse susceptibility, which follows a power law:

$$\chi^{-1}(T) \propto (T - T_K)^{1-\lambda} \quad (2)$$

with $0 \leq \lambda < 1$. The power law in the previous equation is a generalized Curie-Weiss law. Here, T_K is the critical temperature of the ferromagnetic (or ferrimagnetic) clusters [27] that can be estimated from $\lambda = 0$ in the Curie-Weiss regime [72,73], which is equivalent to the Curie-Weiss temperature (θ). The parameter λ appearing in the exponent shows the strength of the GP. The double logarithmic plot of the dc susceptibility against reduced temperature ($t_m = \frac{T}{T_K} - 1$), reproduced in the inset of Fig. 8, shows a linear behavior at low t_m values, and confirm the proposed GP. The fitted value of λ is 0.51 for the as-synthesized $(Fe_{0.25}Mn_{0.75})_2O_3$ and α-Fe_2O_3 sample which is in the range ($0 \leq \lambda < 1$) expected from a system exhibiting the Griffiths phase. It is worth to stress that this parameter is found in the analyses for both phases. Therefore, its value should be underestimated when compared to system with only $(Fe_{0.25}Mn_{0.75})_2O_3$ phase. The solid red line in the inset of Fig. 8 represents the best fit of the χ^{-1} versus T data using Eq. 2, in the range of $5K < T < T_G$. Actually, Eq. 2 represents the temperature dependence of the order parameter (χ^{-1}) in the context of the classical Landau second-order phase transition, with the critical exponent ($\delta = 1$-λ) very much close to ½ [74].

3.7. Magnetic resonance

The MR spectra obtained from the as-synthesized sample at a fixed frequency of 9.50 GHz, in the temperature range of 4.3–293 K are presented in Fig. 9. Throughout this temperature range, a strong and broad resonance signal, with a nearly symmetrical shape, can be observed. This shape is strictly Lorentzian, suggesting a strong interaction between metal ions through the exchange interaction [75]. Moreover, it suggests that the majority $(Fe_{0.25}Mn_{0.75})_2O_3$ phase dominate the spectra. By utilizing $g = h\nu/\mu_B H_R$, where ν denotes the spectrometer's operating frequency (9.50 GHz), μ_B represents the Bohr magneton and H_R represents the extracted MR field, the temperature dependence of the extracted g-values can be plotted, as shown in the inset of Fig. 9. The g-values for the as-synthesized $(Fe_{0.25}Mn_{0.75})_2O_3$ nanocrystals have been found to decrease systematically with increasing temperature, in agreement with the behavior found to perovskites compounds [76,77]. This behavior is largely attributed to a decreasing of the magnetic moments occurring as the temperature rises [27,78]. Specifically, these values decreased from (2.93 ± 0.01) at 50 K to (2.18 ± 0.01) at 300 K.

The inset of Fig. 10 shows H_R vs T, where the vertical dotted black lines indicate T_C, $2T_C$, and T_G temperatures. For $T_G < T < 300K$, the majority $(Fe_{0.25}Mn_{0.75})_2O_3$ phase is paramagnetic and H_R reduces smoothly with decreasing T, due to the enhancement of the magnetic moment [28,78]. For $2T_C < T < T_G$, the $(Fe_{0.25}Mn_{0.75})_2O_3$ phase is still in the paramagnetic state but with the presence of clusters formed at T_G, and H_R decreases sharply due to the enhancement of the magnetic moment and the presence of these clusters. Importantly, the Griffiths-like phase is an intermediate state between the disordered paramagnetic and the ordered ferromagnetic (or ferrimagnetic) state, where it begins to appear magnetic interaction between the FM (or ferrimagnetic) clusters. In the study of $FeMnO_3$ nanoparticles prepared by mechanosynthesis method, Rayaprol et al. [28] showed that at $T \sim 2T_C$ a change in the unit volume cell occurred, and they argued that there is a strong coupling between the structure and the magnetic ordering occurring at T_C, provoking large variations of magnetic entropy in this temperature range. Although another method of synthesis has been herein employed, H_R for $T < 2T_C$ also reduces sharply while decreasing the temperature, confirming that the as-synthesized sample can also show similar behavior on H_R from 66 K ($2T_C$) down to 4.2 K. Therefore, this sharp drop is attributed to the increasing magnetic interaction influenced by structural changes and long-range ferrimagnetic coupling as the system approaches T_C, as well as the spin-glass-like behavior occurring at the surface of the nanoparticles. Fig. 10 shows the variation of peak-to-peak line width (ΔH_{pp}) as function of temperature for the $(Fe_{0.25}Mn_{0.75})_2O_3$ nanocrystals, showing a sharp peak at T_{max} = 42 K (~1.27 T_C), where T_{max} is assigned to the temperature where the ΔH_{pp} is maximum. It is known that for systems showing spin-glass-like behavior, ΔH_{pp} presents noticeable broadening below the spin-glass temperature [79,80]. As shown in Fig. 10, higher value for T_{max} (43 K) while compared to T_C (33 K) is attributed to a surface spin-glass-like

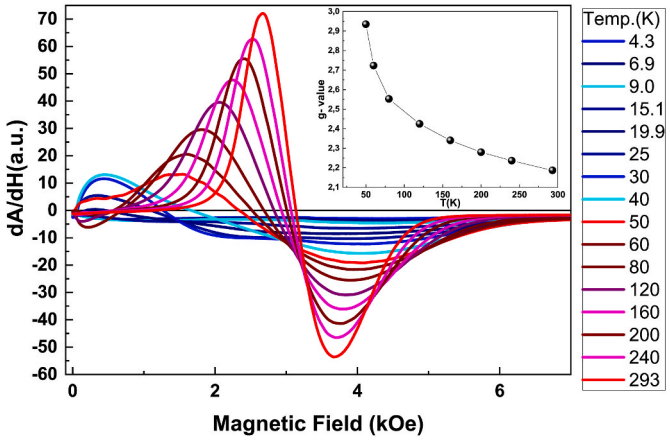

Fig. 9. X-band MR spectra, representing the first derivate of the absorption, recorded from the as-synthesized sample. The spectra were recorded at various temperatures, ranging from 4.3 K to 293 K. The temperature dependence of the g-factor is also plotted in the inset (the solid line is just to guide the eyes).

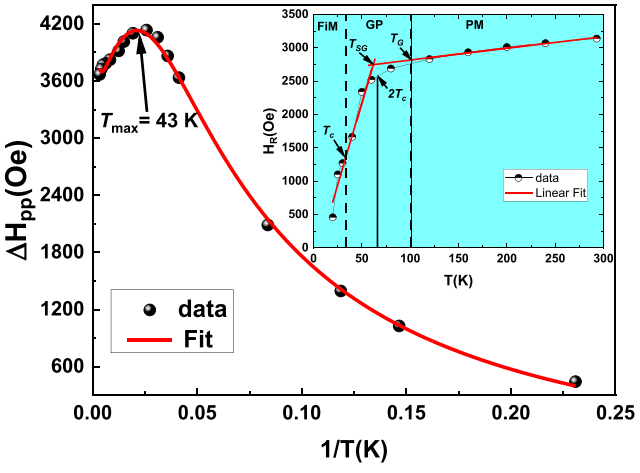

Fig. 10. Experimental values of the magnetic resonance linewidth (ΔH_{pp}) tracked as a function of temperature (T), as indicated by the solid black symbols. The solid red line represents the best fit using Eq. (5). The inset shows the temperature dependence of the resonance field (solid black-white symbols).

behavior of $(Fe_{0.25}Mn_{0.75})_2O_3$ nanocrystals.

Actually, the study of spin-glass-like systems has relied on the temperature dependence of ΔHpp to obtain information about the spin freezing phenomenon and the corresponding freezing temperature (T_f). Recently, an exponential relationship between ΔH_{pp} and T for diluted magnetic semiconductors exhibiting spin-glass behavior has been proposed [81]:

$$\Delta H_{pp} = \Delta H_{\infty} + \Delta H_0(1 - \theta / T)e^{-(T_f/T)} \quad (3)$$

The above-presented relationship incorporates parameters such as ΔH_0 and ΔH_{∞}, which describes ΔH_{pp} respectively at low and high temperatures, and correlates with the concentration of magnetic ions and the dominant magnetic interaction above the transition temperature. The Curie-Weiss temperature (θ) is included in the pre-exponential term, whereas the exponential term allows for determination of the freezing temperature (T_f). Black symbols in Fig. 10 represent the temperature dependence of ΔH_{pp}, with the experimental data fitted to Eq. (3) in the low temperature region, up to 50 K. While Eq. (3) successfully fits the ΔH_{pp} versus T data below 50 K, it fails to account for the experimental data above this temperature. Notably, the ΔH_{pp} values systematically decrease from about 4200 Oe to about 3600 Oe as the temperature is increased from about 50 K to 300 K, representing the opposite trend observed below about 50 K. Importantly, below and above this temperature (50 K), the concavity is upward and downward respectively, signaling a remarkable change in the dominant magnetic behavior.

A key issue in the present study was to analyze the ΔH_{pp} versus T data in the whole temperature range (4.3 K–293 K). In order to accomplish this goal, an additional term $\Delta H_{spm} \tanh(T_{spm}/T)$ was included into Eq. (3) [82]:

$$\Delta H_{pp} = \Delta H_{\infty} + \Delta H_0(1 - \theta / T)e^{-(T_f/T)} + \Delta H_{spm} \tanh(T_{spm} / T) \quad (4)$$

This extra term has proven to be successful in describing the ΔHpp of superparamagnetic particles in a wide range of temperature. Actually, it is related to thermally-induced jumps between two energy minima, which correspond to two distinct orientations of nanoparticle's magnetic moment with respect to the easy axis of magnetization [83,84]. The third term (extra term) on right-hand side of Eq. (4) includes the pre-factor $\Delta H_{spm} = 5g\beta Sn/R^3$, with S, n and R representing the effective spin of the magnetic center, number of magnetic centers inside the superparamagnetic particle and average particle-particle distance, respectively. Also, included into the extra term is a characteristic temperature $T_{spm} = \Delta E/2k_B$, where ΔE is the energy barrier between the two orientations of the nanoparticle's magnetic moment. The solid red line in Fig. 10 represents the best fit of the experimental data while using Eq. (4), with the following fitted values: $\Delta H_{\infty} = (358 \pm 13)$ Oe, $\Delta H_0 = (84 \pm 2)$ Oe, $\theta = (-150 \pm 5)$ K, $T_f = (5.1 \pm 0.1)$ K, $\Delta H_{spm} = (3849 \pm 10)$ Oe, and $T_{spm} = (1194 \pm 5)$ K. Some of these values can be compared with the values obtained experimentally, as instance $\theta = -177$ K (see legend of Figs. 8) and 948 K $\leq T_N \leq$ 963 K obtained for bulk α-Fe_2O_3 [85]. Higher value obtained for T_{spm} should be related to the nanosized characteristic of α-Fe_2O_3 particles. Importantly, it is herein claimed that the extra term included into Eq. (4) describes mainly the contribution of the secondary phase, namely the superparamagnetic hematite (estimated XRD mean size of 8 nm), being dominant at high temperatures (above 50 K), although contributing to a relatively small change in the ΔH_{pp} values, roughly from 3600 Oe to 4200 Oe. Broadening of the MR line while lowering the temperature of superparamagnetic hematite has been widely reported in the literature [86–88]. The successful fitting of the data in the full temperature range of investigation has allowed for a better understanding of the model picture. Overall, the findings have provided valuable insights into the behavior of magnetic nanoparticles at varying temperatures.

Indeed, the present report emphasizes the applicability of the MR technique, while using the ΔH_{pp} versus T data, to unveil the magnetic contributions of a multi-phase nanomaterial presenting distinct magnetic ordering. As indicated by both Mössbauer and XRD data evaluation, the as-synthesized sample comprises mainly two distinct nanophases; the majority (~86 mol%) iron manganese trioxide $(Fe_{0.25}Mn_{0.75})_2O_3$ phase, with mean size around 48 nm, and the minority (~14 mol%) hematite (α-Fe_2O_3) phase with mean size around 8 nm. Typically, different iron oxide nanophases (e.g. iron sulfate, iron oxide, Cd/Zn/Cu/Ni/Mn-ferrite), pristine or surface-dressed, synthetic or extracted from living organisms, present broad MR lines (up to about 4 kOe) and resonance field below about 3.5 kOe [82,83,86,89–92]. Therefore, it is not surprising that the majority $(Fe_{0.25}Mn_{0.75})_2O_3$ phase dominates the MR spectra shape in the wide temperature range of our investigation (4.3–293 K). Nevertheless, the signature of the minority hematite phase is clearly identified in the temperature dependence of ΔH_{pp} above about 50 K, as described by Eq. (4). Whereas the larger (48 nm) magnetic phase (iron manganese trioxide) dominates the ΔH_{pp} trend in the lower temperature range (below about 50 K) the smaller (8 nm) magnetic phase (hematite) contributes remarkably to the ΔH_{pp} trend in the higher temperature range (above about 50 K). It is worth noting that the spin-glass-like behavior should be concentrated at the surface of the nanocrystals (~0.6 nm tick), whereas the core can be magnetic, as reported in other magnetic nanoparticles [82,93]. Moreover, it is not completely ruled out that the surface spin-glass-like behavior can also occur for α-Fe_2O_3 nanoparticles. The third term on the right hand-side of Eq. (4) accounts for the magnetic behavior of the hematite phase, with negligible increment below 60 K, but with non-negligible contribution above 60 K. Therefore, it is not surprising that Eq. (3) can fit nicely the ΔH_{pp} versus T data below about 60 K and fails to perform the fitting in the whole temperature range (4.3–293 K). Likewise, it is not surprising the need of an extra term to account for the superparamagnetic contribution of the hematite phase above 60 K, as included into Eq. (4). Moreover, as the temperature drops below 60 K, it is claimed that a phase transition occurs from a continuous paramagnetic phase to a spin-glass-like phase in the shell layer of the $(Fe_{0.25}Mn_{0.75})_2O_3$ phase. Regarding a rough estimation of the start of this transition, two linear fits have been carried out for H_R vs T, one of them from 20 up to 50 K and the other from 120 to 295 K, where the intersection of these lines was determined as spin-glass temperature $T_{SG} = 60$ K (see inset of Fig. 10). This transition extends down to a value of $T_f = 5.1 \pm 0.1$ K, below which the spins in the shell layer become completely frozen in a specific configuration across the surface of the sample. The linear behavior emphasized in the inset of Fig. 10, namely H_R vs T, has been reported in the literature while associating the slope of straight line with the nanoparticle size [92,93]. Extra evidence of the spin-glass-like characteristic of the $(Fe_{0.25}Mn_{0.75})_2O_3$ nanoparticles' shell layer is the upshift of the g-value while lowering the temperature of the sample, particularly below about 60 K (see inset of Fig. 9). Presence of oxygen vacancies at surface of bixbyite phase, evidenced by XPS measurements, should decrease the indirect exchange coupling mediated by oxygen atoms (super-exchange interaction [94]) between the 3d ions. However, the question about if the spin-glass-type transition found in this work is from a conventional spin-glass or cluster spin-glass would require the determination of the critical exponents [95], and are beyond of the scope of this work. The observed weakening of the magnetic interactions between 3d ions in $FeMnO_3$ nanocrystals suggests a tendency towards spin glass behavior at low temperatures. This weakening, potentially due to structural disorder or changes in ion connectivity within the nanocrystals, reduces the effectiveness of magnetic ordering and promotes the emergence of a spin glass phase, characterized by a frozen, disordered magnetic state without long-range order. It is worth mentioning that high g-values are characteristic of magnetically isolated transition metal ions in a low-symmetry environment, attributed to the presence of relatively strong crystalline fields due to the lack of symmetry translation, as reported in the literature [94].

4. Conclusions

This research focuses on examining the structure and magnetic properties of a nanostructured material initially labeled $FeMnO_3$, synthesized using the sol-gel technique. While using Mössbauer spectroscopy and conducting Rietveld refinement of the X-ray diffraction data, the compound's composition was accurately determined with a majority (94 wt%) bixbyite phase $(Fe_{0.25}Mn_{0.75})_2O_3$. Additionally, a minority hematite phase (6 wt%) was assessed. HRTEM measurements of interplanar distances, conducted in specific zones, validate the presence of $FeMnO_3$ and hematite phases. Raman spectroscopy confirmed the characteristic vibrational bands of the majority phase. X-ray photoelectron spectroscopy revealed oxygen vacancies at the surface of $(Fe_{0.25}Mn_{0.75})_2O_3$ nanoparticles, with varying oxidation states (Fe^{3+}, Fe^{2+}, Mn^{3+}, and Mn^{4+}). The X-band magnetic resonance data showed a prominent and broad resonance line across the temperature range (4.3 K $\leq$ T $\leq$ 300 K), predominantly influenced by the bixbyite phase. Notably, a decrease in the g-value from 2.93 $\pm$ 0.01 at 50 K to 2.18 $\pm$ 0.01 at 300 K was observed. The temperature dependence of the resonance field and linewidth indicated surface spin-glass behavior, particularly evident around 40–50 K. Below approximately 50–60 K, a transition from paramagnetic to spin-glass-like behavior was noted in the shell's spin system of $(Fe_{0.25}Mn_{0.75})_2O_3$ nanoparticles, with a critical temperature estimated at 43 $\pm$ 1 K. Above 50 K, the resonance linewidth's temperature dependence was notably influenced by the superparamagnetic minority phase. Zero-field-cooled and field-cooled data exhibited significant irreversibility, with a peak in the ZFC curve around 33 K, indicative of a paramagnetic-ferrimagnetic transition in the majority phase.

CRediT authorship contribution statement

John C. Mantilla: Writing – review & editing, Writing – original draft, Methodology, Investigation, Formal analysis, Data curation, Conceptualization. **Luiz C.C.M. Nagamine:** Writing – review & editing, Writing – original draft, Methodology, Investigation, Formal analysis, Data curation, Conceptualization. **Daniel R. Cornejo:** Writing – original draft, Formal analysis, Data curation, Conceptualization. **Renato Cohen:** Methodology, Investigation, Data curation. **Wesley de Oliveira:** Methodology, Formal analysis, Data curation. **Paulo E.N. Souza:** Methodology, Investigation, Data curation. **Sebastião W. da Silva:** Methodology, Formal analysis, Data curation. **Fermin F.H. Aragón:** Writing – original draft, Methodology, Investigation, Formal analysis, Data curation. **Pedro L. Gastelois:** Writing – original draft, Methodology, Investigation, Formal analysis, Data curation. **Paulo C. Morais:** Writing – review & editing, Writing – original draft, Investigation, Formal analysis, Data curation, Conceptualization. **José A.H. Coaquira:** Writing – review & editing, Writing – original draft, Methodology, Investigation, Formal analysis, Data curation, Conceptualization.

Declaration of competing interest

The authors declare the following financial interests/personal relationships which may be considered as potential competing interests:

John C. Mantilla reports financial support, administrative support, article publishing charges, equipment, drugs, or supplies, statistical analysis, travel, and writing assistance were provided by Federal University of Uberlandia. The authors whose names are listed immediately below certify that they have NO affiliations with or involvement in any organization or entity with any financial interest (such as honoraria; educational grants; participation in speakers' bureaus; membership, employment, consultancies, stock ownership, or other equity interest; and expert testimony or patent-licensing arrangements), or non-financial interest (such as personal or professional relationships, affiliations, knowledge or beliefs) in the subject matter or materials discussed in this manuscript. If there are other authors, they declare that they have no known competing financial interests or personal relationships that could have appeared to influence the work reported in this paper. If there are other authors, they declare that they have no known competing financial interests or personal relationships that could have appeared to influence the work reported in this paper.

Data availability

No data was used for the research described in the article.

Acknowledgements

Authors acknowledge the *Laboratório Multiusuário de Microscopia de Alta Resolução* (Labmic/UFG), IF/UnB and Laboratory of Crystallography, IF/USP for XRD measurements. John C. Mantilla acknowledges partial financial support from Brazilian National Research Council (CNPq Grant # 101441/2022-3).

References

[1] A.V. Trukhanov, V.A. Turchenko, V.G. Kostishin, F. Damay, F. Porcher, N. Lupu, B. Bozzo, I. Fina, S. Polosan, M.V. Silibin, M.M. Salem, D.I. Tishkevich, S. V. Trukhanov, The origin of the dual ferroic properties in quasi-centrosymmetrical $SrFe_{12-x}In_xO_{19}$ hexaferrites, J. Alloys Compd. 886 (2021) 161249, https://doi.org/10.1016/j.jallcom.2021.161249.

[2] V.A. Turchenko, S.V. Trukhanov, V.G. Kostishin, F. Damay, F. Porcher, D. S. Klygach, M.G. Vakhitov, D. Lyakhov, D. Michels, B. Bozzo, I. Fina, M. A. Almessiere, Y. Slimani, A. Baykal, D. Zhou, A.V. Trukhanov, Features of structure, magnetic state and electrodynamic performance of SrFe12-xInxO19, Sci. Rep. 11 (2021) 18342, https://doi.org/10.1038/s41598-021-97684-8.

[3] V. Markovich, A. Wisniewski, H. Szymczak, Chapter one- magnetic properties of perovskites manganite and their modifications, Handb. Magn. Mater. 22 (2014) 1–201, https://doi.org/10.1016/B978-0-444-63291-3.00001-5.

[4] W. Eerenstein, N.D. Mathur, J.F. Scott, Multiferroic and magneto electric materials, Nature 442 (2006) 759–765, https://doi.org/10.1038/nature05023.

[5] S.V. Trukhanov, I.O. Troyanchuk, M. Hervieu, H. Szymczak, K. Bärner, Magnetic and electrical properties of $LBaMn_2O_{6-\gamma}$ (L = Pr, Nd, Sm, Eu, Gd, Tb) manganites, Phys. Rev. B 66 (2002) 184424, https://doi.org/10.1103/physrevb.66.184424, 10.

[6] J. Mantilla, M. Morales, W. Venceslau, L. Corredor, P.C. Morais, F.F.H. Aragon, S. W. Sebastião, J.A. Coaquira, Field-driven spin reorientation in $SmMnO_3$ polycrystalline powders, J. Alloys Compd. 845 (2020) 156327, https://doi.org/10.1016/j.jallcom.2020.156327, 7.

[7] S.V. Trukhanov, I.O. Troyanchuk, N.V. Pushkarev, H. Szymczak, Magnetic properties of anion-deficient $La_{1-x}Ba_xMnO_{3-x/2}$ ($0 \leq x \leq 0.30$) manganites, J. Exp. Theor. Phys. 96 (2003) 110–117, https://doi.org/10.1134/1.1545390.

[8] P. Tiwari, C. Rath, Evolution of structure and magnetic properties of stoichiometry and oxygen rich $LaMnO_3$ nanoparticles, J. Magn. Magn Mater. 441 (2017) 635–641, https://doi.org/10.1016/j.jmmm.2017.06.020.

[9] Z. Xi, W. Yang, J. Qi, Y. Hu, cells with better electronic properties via pre heating assisted onestep deposition method, Nanoscale Res. Lett. 15 (2020) 1–8, https://doi.org/10.1186/s11671-020-03407-9.

[10] S.V. Trukhanov, L.S. Lobanovski, M.V. Bushinsky, V.A. Khomchenko, V. V. Fedotova, I.O. Troyanchuk, H. Szymczak, Microstructure evolution and magnetoresistance of the A-site ordered Ba-doped manganites, Semiconductors 41 (2007) 507–511, https://doi.org/10.1134/S1063782607050041.

[11] B. Aïssa, A. Ali, F. El-Mellouhi, Oxide and organic–inorganic halide perovskites with plasmonics for optoelectronic and energy applications: a contributive Review, Catalysts 11 (2021) 1–31, https://doi.org/10.3390/catal11091057.

[12] A.V. Trukhanov, M.A. Almessiere, A. Baykal, Y. Slimani, E.L. Trukhanova, A. V. Timofeev, V.G. Kostishin, S.V. Trukhanov, M. Sertkol, A. Ul-Hamid, Correlation between the composition, structural parameters and magnetic properties of spinel-based functional nanocomposites, Nano-Struct. Nano-Objects 33 (2023) 100941, https://doi.org/10.1016/j.nanoso.2023.100941.

[13] A.M. Henaish, M.A. Darwish, O.M. Hemeda, I.A. Weinstein, T.S. Soliman, A. V. Trukhanov, S.V. Trukhanov, D. Zhou, A.M. Dorgham, Structure and optoelectronic properties of ferroelectric PVA-PZT nanocomposites, Opt. Mater. 138 (2023) 113402, https://doi.org/10.1016/j.optmat.2022.113402.

[14] W. Travis, E.K. Glover, H. Bronstein, D.O. Scanlon, G. Palgrave, On the application of the tolerance factor to inorganic and hybrid halide perovskite: a revised system, Chem. Sci. 7 (2016) 4548–4556, https://doi.org/10.1039/c5sc04845a.

[15] V.M. Goldschmidt, Die Gestze der Krystallochemie, vol. 14, 1926, pp. 477–485.

[16] D.J. Singh, W.E. Pickett, Pseudo gaps, Jahn-Teller distortions, and magnetic ordering manganite perovskites, Phys. Rev. B57 (1998) 88–91, https://doi.org/10.1103/PhysRevB.57.88.

[17] S. Jarin, Y. Yuan, M. Zhang, M. Hu, M. Rana, S. Wang, R. Knibbe, Predicting the crystal structure and lattice parameters of the perovskite materials via different Machine, learning models based on basic atom properties, Crystals 12 (2022) 1570–1591, https://doi.org/10.3390/cryst12111570.

[18] W. Xia, Z. Pei, K. Leng, X. Zhu, Research progress in rare earth-doped perov- skite manganite oxide nanostructures, Nanoscale Res. Lett. 15 (9) (2020) 1–55, https://doi.org/10.1186/s11671-019-3243-0.

[19] J. Shang, H. Xiaoyu, S. Whang, Z. Ye, Unraveling the valence states of manganese ions an the effects of composition variation and post-processing in YGG_{1-x}-$LuGG_x$: Mn garnet optical sensor, Chem. Eng. J. 411 (2021) 128448, 11.

[20] J. Fontcuberta, Multiferroic RMnO3 thin films, Compt. Rendus Phys. 16 (2015) 204–226, https://doi.org/10.1016/j.crhy.2015.01012.

[21] R. Nikam, S. Rayaprol, P.S. Goyal, P.D. Babu, S. Radha, V. Siruguri, Structural and magnetic properties of Fe-doped Mn_2O_3 orthorhombic bixbyite, J. Super- cond. Novel Mag. 31 (2018) 2179–2185, https://doi.org/10.1007/s10948-017-4464-z.

[22] S.V. Trukhanov, A.V. Trukhanov, L.V. Panina, V.G. Kostishyn, V.A. Turchenko, E. L. Trukhanova, AnV. Trukhanov, T.I. Zubar, V.M. Ivanov, D.I. Tishkevich, D. A. Vinnik, S.A. Gudkova, D.S. Klygach, M.G. Vakhitov, P. Thakur, A. Thakur, Y. Yang, Temperature evolution of the structure parameters and exchange interactions in $BaFe_{12-x}In_xO_{19}$, J. Magn. Magn Mater. 466 (2018) 393–405, https://doi.org/10.1016/j.jmmm.2018.07.041.

[23] A. Aziz, E. Ahmed, M.N. Ashiq, M.A. Khan, N. Karamat, I. Ali, Structural, electrical, dielectric and magnetic properties of Mn-Nd substituted $CoFeO_3$ nano sized multiferroics, Prog. Nat. Sic: Mat.Int. 26 (2016) 325–333.

[24] K. Cao, H. Liu, X. Xu, Y. Wang, L. Jiao, $FeMnO_3$: a high-performance Li-ion battery anode material, Chem. Commun. 52 (2016) 11414, https://doi.org/10.1039/C6CC04891A, 4.

[25] H. Bin, Z. Yao, S. Zhu, C. Zhu, H. Pan, Z. Chen, C. Wolverton, Di Zhang, A high-performance anode material based on $FeMnO_3$/graphene composite, J. Alloys Compd. 695 (2017) 1223–1230.

[26] L. Pauling, M.D. Shappell, The crystal structure of bixbyite and the C-modifica- tion of the sesquioxides, Z. Kristallogr. 75 (1930) 128–142, https://doi.org/10.1515/zkri-1930-0109.

[27] S. Rayaprol, V.R. Kaushik, Magnetic and magnetocaloric properties of $FeMnO_3$, Ceram. Int. 41 (2015) 9567–9571, https://doi.org/10.1016/j.ceramint.2015.04.017.

[28] S. Rayaprol, R.A.P. Ribeiro, K. Singh, V.R. Reddy, S.D. Kaushik, S.R. Lazaro, Experimental and theoretical interpretation of magnetic ground state of $FeMnO_3$, J. Alloys Compd. 774 (2019) 290–298, https://doi.org/10.1016/j.jall-com.2018.09.367.

[29] T.P. Ioannis, A. Ioakeimidis, I. Vamvasakis, P. Eleftheriou, G.S. Armatas, S. A. Choulis, All-Inorganic p−n heterojunction solar cells by solution combustion synthesis using N-type $FeMnO_3$ perovskite photoactive layer, Front. Chem. 9 (2021) 1–11, https://doi.org/10.3389/fchem.2021.754487.

[30] Z.Z. Vasiljevic, M.P. Dojcinovic, J.B. Krstic, V. Ribic, N.B. Tadic, M. Ognja- novic, S. Auger, J. Vidicf, M.V. Nikolic, Synthesis and antibacterial activity of iron manganite ($FeMnO_3$) particles against the environmental bacterium bacillus subtilis, RSC Adv. 10 (2020) 13879–13888.

[31] R.E. El-Shater, H. El Shimy, S.A. Saafan, M.A. Darwish, D. Zhou, K.C.B. Naidu, M. U. Khandaker, Z. Mahmoud, A.V. Trukhanov, S.V. Trukhanov, F. Fakhry, Fabrication of doped ferrites and exploration of its structure and magnetic behavior, Mater. Adv. 4 (2023) 2794–2810, https://doi.org/10.1039/d3ma00105a.

[32] T.I. Zubar, V.M. Fedosyuk, S.V. Trukhanov, D.I. Tishkevich, D. Michels, D. Lyakhov, A.V. Trukhanov, Method of surface energy investigation by lateral AFM: application to control growth mechanism of nanostructured NiFe films, Sci. Rep. 10 (2020) 14411, https://doi.org/10.1038/s41598-020-71416-w.

[33] S.A. De la Torre, J.C.R. Aquino, A.F. Carlos-Chilo, J.A. Guerra, J.A.H. Coaquira, D. G. Pacheco, J.F. Felix, J.L. Solis, F.F.H. Aragon, Enhancing the photoconductivity and gas sensing performance of ToO2/SnO2 heterostructures tuned by thickness of SnO2 upper layer, Appl. Surf. Sci. 613 (2023) 156028.

[34] S.A. Barbosa, O.J.B. Marques, E.L.T. França, F.L.A. Machado, J.C. Mantilla, Magnetic properties of the Double perovskites $Sm_2Mn_{1+x}Co_{1-x}O_6$ (x= 0.00, 0.05, 0.12 and 0.26), J. Phys. Condens. Matter 32 (2019) 105803–105810, https://doi.org/10.1088/1361-648X/ab5988.

[35] I.A. Campbell, Spin glasses and reentrant alloys, Hyperfine Interact. 27 (1986) 15–22, https://doi.org/10.1007/BF02354740.

[36] K. Ehrensberger, A. Frei, P. Kuhn, H.R. Oswald, P. Hug, Comparative experi- mental investigations of the water-splitting reaction with iron oxide $Fe_{1-y}O$ and iron manganese oxides $(Fe_{1-x}Mn_x)_{1-y}O$, Solid State Ionics 78 (1995) 151–160, https://doi.org/10.1016/0167-2738(95)00019-3.

[37] D. Seifu, A. Kebede, F.W. Oliver, E. Hoffman, E. Hammond, C. Wynter, A. An- ing, L. Takacs, I.L. Siu, J.C. Walker, G. Tessema, M.S. Seehra, Evidence of ferromagnetic ordering in $FeMnO_3$ produced by mechanical alloying, J. Magn. Magn Mater. 212 (2000) 178–182.

[38] H. Le Roux, Mossbauer study of paramagnetic and magnetic components in an uncalcined iron manganese oxide powder, J. Phys. Condens. Matter 2 (1990) 3391–3398, https://doi.org/10.1088/0953-8984/2/14/023.

[39] P.S. Satish, M.S. Lad, K.V. Kandam, S.A.M. Tofail, N.D. Thorat, V.M. Khot, Application of $Mn_xFe_{1-x}Fe_2O_4$ (x = 0−1) nanoparticles in magnetic fluid hy- perthermia: correlation with cation distribution and magnetostructural proper- ties, ACS Omega 7 (2022) 44187–44198.

[40] S. Ponce, M.A. Peña, J.L.G. Fierro, Surface properties and catalytic performance in methane combustion of Sr-substituted lanthanum manganites, Appl. Catal., B: Environmental. 24 (2000) 193–205, https://doi.org/10.1016/S0926-3373(99)00111-3.

[41] A.E. Stanciu, G. Schinteie, A.C. Kuncser, C. Locovei, L. Trupina, N. Iacob, A. Leca, B.V. Borca, Kuncser, magnetic properties of nanosized Fe and FeCo sys- tems on trenched Mo templates, Coatings 12 (2022) 1366–1382, https://doi.org/10.3390/coatings12091366.

[42] S.D. Jiang, T. Eggers, O. Thiabgoh, D. W. Xing, W. D. Fei, H.X. Shen, J. S. Liu, J. R. Zhang, W. B. Fang, J. F. Sun, H. Srikanth, M. H. Phan. Relating surface roughness and magnetic domain structure to giant magneto-impedance of Co-rich melt-extracted microwaves. Sci. Rep.. 7: 46253. https://10.1038/srep46253.

[43] E. Bazhenova, K. Honkala, Screening the bulk properties and reducibility of Fe-doped Mn_2O_3 from first principles calculations, Catal. Today 285 (2017) 104–113, https://doi.org/10.1016/j.cattod.2017.02.004.

[44] H.M. Rietveld, Line profiles of neutron powder-diffraction peaks for structurere finement, Acta Cryst 22 (1967) 151–152, https://doi.org/10.1107/S0365110X67000234.

[45] B.H. Toby, R.B. Von Dreele, The genesis of a modern open source-all purpose crystallography software package, J. appl. Cryst. 46 (2013) 544–549.

[46] E. De Grave, R.E. Vandenberghe, Mössbauer effect study of the spin structure in natural hematites, Phys. Chem. Miner. 17 (1990) 344–352, https://doi.org/10.1007/BF00200130.

[47] N. Amin, S. Arajs, Morin temperature of annealed submicronic α-Fe_2O_3 particles, Phys. Rev. B 35 (1987) 4810–4811, https://doi.org/10.1103/PhysRevB.35.4810.

[48] M. Tadic, D. Markovíc, V. Spasojevíc, V. Kusigerki, M. Remskar, J. Pirnat, Z. Jaglicíc, Synthesis and magnetic properties of concentrated α-Fe2O3 nanoparti- cles in a silica matrix, J. Alloys Compd. 441 (2007) 291–296, https://doi.org/10.1016/j.jallcom.2006.09.099.

[49] J. Nell, H. Pollak, J.A. Lodya, Intersite cation portioning in natural and synthetic alpha-$(Fe,Mn)_2O_3$ (bixbyite) solid solution determined from ^{57}Fe Mossbauer spectroscopy, Hyperfine Interact. 91 (1994) 601–605, https://doi.org/10.1007/BF02064577.

[50] B. Kolk, A. Albers, G.R. Hearne, H. Le Roux, H. Evidence of a new structural phase of manganese-iron oxide, Hyperfine Interact. 42 (1988) 1051–1054, https://doi.org/10.1007/BF02395571.

[51] D. Kubániováa, L. Kubíčkováa, T. Kmječa, K. Závětaac, D. Nižňanskýb, P. Brázdac, M. Klementovác, J. Kohou, Hematite: Morin temperature of nanoparticles with different size, J. Magn. Magn Mater. 475 (2019) 611–619, https://doi.org/10.1016/j.jmmm.2018.11.126.

[52] A. Monshi, M.R. Foroughi, M.R. Monshi, Modified Scherrer equation to esti- mate more accurately Nano-Crystallite size using XRD, World J. Nano Sci. Eng. 2 (2012) 154–160, https://doi.org/10.4236/wjnse.2012.23020.

[53] S. Geller, Structures of α-Mn_2O_3, $(Mn_{0.983}Fe_{0.017})_2O_3$ and $(Mn_{0.37}Fe_{0.63})_2O_3$ and relation to magnetic ordering, Acta Crystallogr. B27 (1971) 821.

[54] M.V. Abrashev, N.D. Tadorov, J. Geshev, Raman spectra of R_2O_3 (R-rare earth) sesqui oxides with C-type bixbyite crystal structure: a comparative study, J. Appl. Phys. 116 (2014) 103508, https://doi.org/10.1063/1.4894775, 1.

[55] Z. Chen, S. Tan, S. Zhang, J. Wang, S. Jin, Y. Zhang, H. Sekine, Size dependence of phonon Raman spectra in Mn_2O_3 nanocrystals, Jpn. J. Appl. Phys. 39 (2000) 6293–6295, https://doi.org/10.1143/JJAP.39.6293.

[56] T. Yamashita, P. Hayes, Analysis of XPS spectra Fe^{2+} and Fe^{3+} ions in oxides Materials, Appl. Surf. Sci. 254 (2008) 2441–2449.

[57] W.B. White, V.G. Keramidas, Vibrational spectra of oxides with the C-type rara earth oxide structure, Spectrochim. Acta, Part A 28 (1972) 501–509, https://doi.org/10.1016/0584-8539(72)80237-X.

[58] L.Q. Wu, Y.C. Li, S.Q. Li, Z.Z. Li, G.D. Tang, W.H. Qi, L. Xue, X.S. Ge, L.L. Ding, Method for estimating ionicities of oxides using O1s photoelectron spec tra, AIP Adv. 5 (2015) 097210, https://doi.org/10.1063/1.4931996, 7.

[59] S.V. Trukhanov, M.V. Bushinsky, I.O. Troyanchuk, H. Szymczak, Magnetic ordering in $La_{1-x}Sr_xMnO_{3-x/2}$ anion-deficient manganites, J. Exp. Theor. Phys. 99 (2004) 756–765, https://doi.org/10.1134/1.1826167.

[60] B.D. Cullity, C.D. Graham, Introduction to Magnetic Materials, second ed., John Wiley & Sons, New Jersey, 2009.

[61] J.M.D. Coey, Magnetism and Magnetic Materials, Cambridge University Press, New York, 2010.

[62] Ying-Ying Xu, Long wang, Tong wu, Rong-Ming Wang, Magnetic properties of α-Fe_2O_3, Rare metals 38 (2019) 14–19.

[63] Y. Takahashi, On the origin of the curie-weiss law of the magnetic susceptibil- ity in itinerant electron ferromagnetism, J. Phys. Soc. Japan 55 (1986) 3553, https://doi.org/10.1143/JPSJ.55.3553, 21.

[64] M. Tadic, M. Panjan, V. Damnjanovic, I. Milosevic, Magnetic properties of hematite (α-Fe_2O_3) nanoparticles prepared by hydrothermal synthesis method, Appl. Surf. Sci. 320 (2014) 183, https://doi.org/10.1016/j.apsusc.2014.08.193.

[65] L.L.D. Sanjeewa, A.S. Sefat, M. Smart, M.A. McGuire, C.D. McMillen, J. Kolis, Synthesis, structure and magnetic properties of $Ba_3M_2Ge_4O_{14}$ (M= Mn and Fe): quasi-one-dimensional zigzag chain compounds, J. Solid State Chem. 283 (2020) 121090–121097, https://doi.org/10.1016/j.jssc.2019.121090.

[66] N. Roth, F. Ye, A.F. May, B.C. Chakoumakos, B.B. Iversen, Magnetic correla- tions and structure in bixbyite across the spin-glass transition, Phys. Rev. B 100 (2019) 144404, https://doi.org/10.1103/PhysRevB.100.144404.

[67] A.H. Hill, P.G. Bruce, A. Harrison, W. Kockelmann, C. Ritter, Neutron diffraction study of mesoporous and bulk hematite α-Fe_2O_3, Chem. Mater. 20 (2008) 4891, https://doi.org/10.1021/cm800009s.

[68] S. Blundell, Magnetism in Condensed Matter, Oxford Academic University Press, London, 2001, https://doi.org/10.1093/oso/9780198505921.001.001.

[69] Yang Xin, Lei Shi, Jiyin Zhao, Xueyou Yuan, Shiming Zhou, Li Hou, Liping Yang, Nature of griffiths phase and ferromagnetic 3d-4f interaction in double –perovskites Dy_2CoMnO_6, J. Alloys Compd. 893 (2022) 162222–162227.

[70] B. Mali, H.S. Nair, T.W. Heitmann, H. Nhalil, D. Antonio, K. Gofryk, S.R. Bhandari, M.P. Ghimire, S. Elizabeth, Re-entrant spin reorientation transition and Griffiths-like phase in antiferromagnetic $TbFe_{0.5}Cr_{0.5}O_3$, Phys. Rev. B 102 (2020) 014418, https://doi.org/10.1103/PhysRevB.102.014418, 10.

[71] S.M. Zhou, Y.Q. Guo, J.Y.Q. Zhao, S.J. Zhao, L. Shi, Nature of short-range ferromagnetic ordered state above Tc in Double perovskite La_2NiMnO_6, Appl. Phys. Lett. 96 (2010) 262507, https://doi.org/10.1063/1.3459141, 3.
[72] J. Lin, P. Tong, D. Cui, C. Yang, S. Lin, B. Wang, W. Tong, L. Zhang, Y. Zou, Unusual ferromagnetic critical behavior owing to short-range antiferromagnetic correlations in antiperovskite $Cu_{1-x}NdMn_{3+x}$ ($0.1 \leq x \leq 0.4$), Sci. Rep. 5 (2015) 7933–7937, https://doi.org/10.1038/srep07933.
[73] A. Karmakar, S. Majumdar, S. Kundu, T.K. Nath, S.A. Giri, A Griffiths-like phase in antiferromagnetic $R_{0.5}Eu_{0.5}MnO_3$ (R = Pr, Nd, Sm), J. Phys. Condens. Matter 25 (2013) 066006, https://doi.org/10.1088/0953-8984/25/6/066006, 8.
[74] W. Jiang, X.Z. Zhou, G. Williams, Correlation between phase competition and the nucleation of a Griffiths-like phase in $(La_{1-y}Pr_y)_{0.7}Ca_{0.3}Mn_{16/18}O_3$, Eu- rophys, Letture 84 (2008) 47009, https://doi.org/10.1209/0295-5075/84/47009, 6.
[75] P.C. Morais, G.M. Ribeiro, A.S. Chaves, EPR study of the ferroelastic phase transition in $CsLiSO_4$, Solid State Commun. 52 (1984) 291–292, https://doi.org/10.1016/0038-1098(84)90828-7.
[76] C.P. Poole, C.P. Poole Jr., Relaxation in Magnetic Resonance, Academic Press Inc., London, 1971.
[77] W.W. Tong, B. Zhang, S. Tan, Y. Zhang, Probability of double exchange between Mn and Fe in $LaMn_{1-x}Fe_xO_3$, Phys. Rev. B 70 (2004) 014422, https://doi.org/10.1103/PhysRevB.70.014422, 6.
[78] S. Harikrishnan, C.M.N. Kumar, S.S. Rao, H.L. Bhat, S.V. Bhat, S. Elizabeth, Electron paramagnetic resonance studies on multiferroic $DyMnO_3$ and $Dy_{0.5}Sr_{0.5}MnO_3$, J. App. Phys. 104 (2008) 023902, https://doi.org/10.1063/1.2955774, 6.
[79] K.H. Wu, Y.C. Chang, H.B. Chen, C.C. Yang, D.N. Horng, Variable temperature electron paramagnetic resonance studies of the NiZn ferrite/SiO_2 nanocomposite, J. Magn. Magn Mater. 278 (2004) 156–163, https://doi.org/10.1016/j.jmmm.2003.12.331.
[80] R.V. Upadhyay, K. Parekh, R.V. Mehta, Spin-glass transition in a model magnetic fluid: electron spin resonance investigation of $Mn_{0.5}Zn_{0.5}Fe_2O_4$ nanoparticles dispersed in kerosene, Phys. Rev. B 68 (2003) 224434, https://doi.org/10.1103/PhysRevB.68.224434, 1.
[81] J.C. Mantilla, W.M. Pontuschka, L.F. Gamarra, V.L. Salvador, S.G. Couto, A. J. Costa-Filho, G.E.S. Brito, V. Sagredo, V. Bindilatti, Magnetic resonance in the $Zn_{1-x}Mn_xIn_2Se_4$ dilute magnetic semiconductor system, J. Phys. Condens. Matter 17 (2005) 2755–2762, https://doi.org/10.1088/0953-8984/17/17/025.
[82] J. Mantilla, F.L. León, M. Marco, P. Souza, R. Pedro, F. Leandro, S.W. Da Silva, J. A. Coaquira, F.F.H. Aragón, P.C. Morais, Evidence of surface spin-glass be- havior in $NiFe_2O_4$ nanoparticles determined using magnetic resonance technique, J. Magn. Magn Mater. 476 (2019) 392–397, https://doi.org/10.1016/j.jmmm.2019.01.001.
[83] P.C. Morais, M.C.L. Lara, K. Skeff Neto, Electron spin resonance in superpara-magnetic particles dispersed in a non-magnetic matrix, Phil. Mag. Lett. 55 (1987) 181–183, https://doi.org/10.1080/09500838708207553.
[84] E.A. Preoteasa, G. Schianchi, D.C. Giori, EPR detection of possible superpara-magnetic polyiron nanoparticles and free radicals in the blood serum of Pa- tients with homozygous β-thalassemia, Appl. Magn. Reson. 45 (2014) 537–571, https://doi.org/10.1007/s00723-014-0540-8.
[85] F. Bodker, M.F. Hansen, K.C. Bender, K. Lefmann, S. Morup, Magnetic proper- ties of hematite nanoparticles, Phys. Rev. B 61 (2000) 6826–6838, https://doi.org/10.1103/PhysRevB.61.6826.
[86] O. Silva, E.C.D. Lima, P.C. Morais, Cadmium ferrite ionic magnetic fluid: mag netic resonance investigation, J. Appl. Phys. 93 (2003) 8456–8458, https://doi.org/10.1063/1.1540165.
[87] D. Niebieskiwiat, R.D. Sánchez, A. Carneiro, L. Morales, M. Vásquez-Mancilla, F. Rivadulla, L.S. Hueso, High-temperature properties of the Sr_2FeMoO_6 double perovskite: electrical resistivity, magnetic susceptibility, and ESR, Phys. Rev. B 62 (2000) 3340–3345, https://doi.org/10.1103/PhysRevB.62.3340.
[88] R.H. Kodama, A.E. Berkowitz, E.J. McNiff, S. Foner, Surface spin disorder in $NiFe_2O_4$ nanoparticles, Phys. Rev. Lett. 77 (1996) 394–397, https://doi.org/10.1103/PhysRevLett.77.394.
[89] A.F. Bakuzis, P.C. Morais, F.A. Tourinho, Investigation of the magnetic anisot- ropy in manganese ferrite nanoparticles using magnetic resonance, J. Magn. Reson. 122 (1996) 100–103, https://doi.org/10.1006/jmra.1996.0184.
[90] E. Wajnberg, D. Acosta-Avalos, L.J. El-Jaik, L. Abraçado, J.L.A. Coelho, A. F. Bakuzis, P.C. Morais, D.M.S. Esquivel, Electron paramagnetic resonance study of the migratory ant Pachycondyla marginata abdomen, Biophys. J. 78 (2000) 1018–1023, https://doi.org/10.1016/S0006-3495(00)76660-4.
[91] G.R.R. Gonçalves, A.R. Pereira, A.F. Bakuzis, K. Skeff Neto, F. Pelegrini, P. C. Morais, Magnetic resonance of zinc- and copper-ferrite ionic magnetic fluids: temperature effects, J. Magn. Magn Mater. 226–230 (2001) 1896–1898, https://doi.org/10.1016/S0304-8853(00)00831-3.
[92] A.R. Pereira, F. Pelegrini, K. Skeff Neto, N. Buske, P.C. Morais, Magnetic reso-nance of field-frozen and zero-field-frozen magnetic fluids, J. Magn. Magn Mater. 272–276 (2004) 2383–2384, https://doi.org/10.1016/j.jmmm.2003.12.1123.
[93] E.M. Yahaiaoui, R. Berger, Y. Servant, J. Kliava, L. Cugunov, A. Mednis, Elec- tron paramagnetic resonance of Fe^{3+} ions in borate glass: computer simulations, J. Phys. Condens. Matter 6 (1994) 9415–9428, https://doi.org/10.1088/0953-8984/6/44/020.
[94] J.B. Goodenough, Theory of the role of covalence in the perovskite-tipe Manganites [La,M(II)]MnO_3, Phys. Rev. 100 (1955) 564.
[95] S. Nair, A.K. Nigam, Critical exponents and the correlation length in the manganite spin glass $Eu_{0.5}Ba_{0.5}MnO_3$, Phys. Rev. B 75 (2007) 214415.